NASA/TP–20230005269

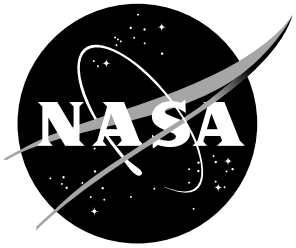

Basic Theory and Operating Principles of Optical Frequency Domain Reflectometry Measurement Systems as Applied to Fiber Bragg Grating Sensors

Jason P. Moore
Langley Research Center, Hampton, Virginia

May 2023

NASA STI Program. . . in Profile

Since its founding, NASA has been dedicated to the advancement of aeronautics and space science. The NASA scientific and technical information (STI) program plays a key part in helping NASA maintain this important role.

The NASA STI Program operates under the auspices of the Agency Chief Information Officer. It collects, organizes, provides for archiving, and disseminates NASA's STI. The NASA STI Program provides access to the NASA Aeronautics and Space Database and its public interface, the NASA Technical Report Server, thus providing one of the largest collection of aeronautical and space science STI in the world. Results are published in both non-NASA channels and by NASA in the NASA STI Report Series, which includes the following report types:

- TECHNICAL PUBLICATION. Reports of completed research or a major significant phase of research that present the results of NASA programs and include extensive data or theoretical analysis. Includes compilations of significant scientific and technical data and information deemed to be of continuing reference value. NASA counterpart of peer-reviewed formal professional papers, but having less stringent limitations on manuscript length and extent of graphic presentations.
- TECHNICAL MEMORANDUM. Scientific and technical findings that are preliminary or of specialized interest, e.g., quick release reports, working papers, and bibliographies that contain minimal annotation. Does not contain extensive analysis.
- CONTRACTOR REPORT. Scientific and technical findings by NASA-sponsored contractors and grantees.
- CONFERENCE PUBLICATION. Collected papers from scientific and technical conferences, symposia, seminars, or other meetings sponsored or co-sponsored by NASA.
- SPECIAL PUBLICATION. Scientific, technical, or historical information from NASA programs, projects, and missions, often concerned with subjects having substantial public interest.
- TECHNICAL TRANSLATION. English-language translations of foreign scientific and technical material pertinent to NASA's mission.

Specialized services also include organizing and publishing research results, distributing specialized research announcements and feeds, providing information desk and personal search support, and enabling data exchange services.

For more information about the NASA STI Program, see the following:

- Access the NASA STI program home page at `http://www.sti.nasa.gov`
- E-mail your question to `help@sti.nasa.gov`
- Phone the NASA STI Information Desk at 757-864-9658
- Write to:
  NASA STI Information Desk
  Mail Stop 148
  NASA Langley Research Center
  Hampton, VA 23681-2199

NASA/TP–20230005269

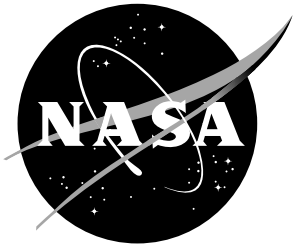

Basic Theory and Operating Principles of Optical Frequency Domain Reflectometry Measurement Systems as Applied to Fiber Bragg Grating Sensors

Jason P. Moore
Langley Research Center, Hampton, Virginia

National Aeronautics and
Space Administration

Langley Research Center
Hampton, Virginia 23681-2199

May 2023

Acknowledgments

For thorough reviews and feedback in the development of this paper, much appreciation is given to Allen Parker and Dr. Patrick Chan of NASA Armstrong Flight Research Center, Dr. Peter Spaeth and Dr. Bill Winfree *(retired)* of NASA Langley Research Center, and Dr. Jeffrey N. Blanton of the Naval Surface Warfare Center Dahlgren *(retired)*.

Available from:

NASA STI Program / Mail Stop 148
NASA Langley Research Center
Hampton, VA 23681-2199
Fax: 757-864-6500

Abstract

Optical frequency domain reflectometer (OFDR) systems provide for the interrogation of hundreds of fiber Bragg gratings (FBGs) within a single optical fiber. The coupling of FBG sensors to an OFDR interrogator results in a highly-distributed measurement system utilizing sensors that are lightweight, immune to electromagnetic interference, and low-profile. This paper presents and explores a basic derivation of OFDR-FBG signals, the processing of those signals, the assembly of a basic OFDR system, an example measurement scenario, and the effects of specific component and configuration changes on interrogator speed, resolution, and accuracy.

1 Introduction

Advantages of fiber optic sensors over electrical counterparts include electromagnetic immunity, lower mass, smaller footprint, and higher bandwidth. Of the many types of fiber optic sensors, the fiber Bragg grating (FBG) continues to be an attractive choice for engineers and researchers. The first report of an in-fiber reflective phenomenon due to a light-induced grated index of refraction along a Ge-doped photosensitive fiber was by Hill *et al.* [1] in 1978, and research of the phenomenon continued through the 1980's. With the introduction of the transverse holography method for manufacturing FBGs by Meltz *et al.* [2] in 1989, the research and development of the FBG as both a sensor and a critical fiber optic communications component intensified. Presently, the FBG continues to be a dominant subject in the field of fiber optics and it has become the sensor of choice for a plethora of fiber optic sensing systems. Too numerous to individually list, examples of the many types of detected/measured physical phenomenon by FBGs and the ever-growing number of FBG demodulation methods are plentiful in literature and summarized well in book form [3, 4].

An FBG is a section of optical fiber in which the index of refraction is periodically modulated to induce a reflective response at a resonance, or "Bragg", wavelength [5]. FBG-based sensing systems typically infer measurements by tracking Bragg wavelength shifts due to fiber-coupled environmental changes such as structural deformation/flexing, temperature, chemical presence, and pressure. In 1998, NASA was issued a patent for a new type of interrogation method and system: the optical frequency domain reflectometer (OFDR) [6]. An OFDR is capable of simultaneously tracking the Bragg wavelength of hundreds of low-reflectivity ($< 0.1\%$) FBGs in a single sensing fiber, making it a highly-distributed fiber optic sensing platform [7]. The technology has seen use in several NASA and non-NASA applications and is now available commercially as both a sensing system and a fiber optic component analyzer [8, 9]. Existing literature provides some explanation of basic theory and operation of the OFDR method; however, there is little attention given to the totality of simplified signal modeling, system analysis, and basic assembly/implementation of an OFDR-FBG sensing system. What follows is a basic derivation of OFDR-FBG signals, the processing of those signals, the assembly of a basic OFDR system, an example measurement scenario, and the effects of specific component and configuration changes on interrogator speed, resolution, and accuracy.

2 Signal Generation

Electric field representation

In this paper, the modeling of optical signals in an OFDR is accomplished via consideration of the electric field component of an electromagnetic wave. A simplified electric field representation of a monochromatic plane wave propagating along an

optical fiber is

$$E = E_0 e^{i(knz - \omega t + \delta)}, \tag{1}$$

where E_0 is the electric field amplitude, k is the free space wavenumber of the field, n is the effective index of refraction of the fiber, z is propagation distance through the fiber, ω is the angular frequency of the light, t is time, and δ is a phase offset. The wavenumber k is explicitly defined as

$$k = \frac{2\pi}{\lambda}, \tag{2}$$

where λ is wavelength, and the angular frequency ω is explicitly defined as

$$\omega = 2\pi f, \tag{3}$$

where f is the light frequency. When representing the light electric field as a propagating monochromatic plane wave as in eq. 1, the power P of the light is proportional to the time-average intensity I of the field, which is proportional to the time-averaged value of the squared electric field:

$$P \propto I \propto EE^* \propto E_0^2. \tag{4}$$

While exact values of power and intensity can be calculated with direct dependence on fiber index of refraction and permittivity, it is not useful in the discussion of this paper to include those calculations, as the exact values are not relevant to the signal analysis presented. Because all optical signals in an OFDR are ultimately detected using photodetectors, which measure power on a time-average basis, and because the speed of light is significantly faster than any phenomenon being measured with an OFDR, it is convenient to omit the ωt term in the complex component of eq. 1. In many cases, the phase offset δ of eq. 1 is also omitted, as it is either assumed to be zero or its exact value is inseparable in the absolute sense from the propagator term knz.

Fiber optic Michelson interferometer

Critical to the modeling and analysis of OFDR operation is an understanding of the output of the fiber optic Michelson interferometer. While the behavior and output of the in-fiber Michelson interferometer is elementary and found in multiple textbooks and articles, it is re-analyzed here in order to form the output signal in the terms and variables of the monochromatic plane wave as defined in eqs. 1-4. An example of a simple dual-leg in-fiber Michelson interferometer is shown in figure 1.

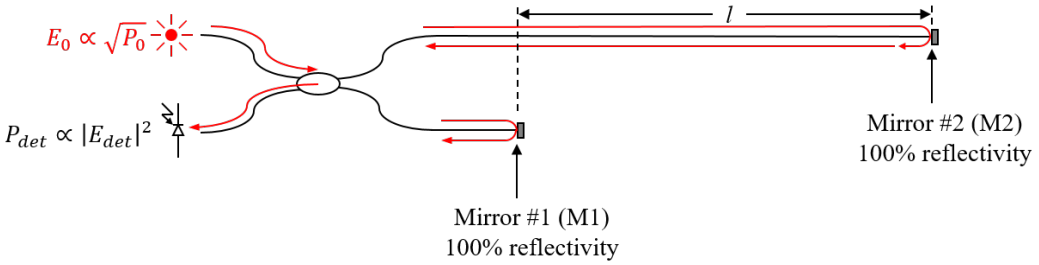

Figure 1. Dual-leg in-fiber Michelson interferometer.

In the simple arrangement of figure 1, a continuous-output, wavelength-sweeping source laser launches light with power P_0 into one leg of a 50/50 coupler where it is equally split between two separate lengths of mirror-terminated fiber. The back-reflected light is half-coupled through the coupler to a photodetector termination. For an electric field of amplitude E_0 launched at the laser, the electric field returning to the detector from the shorter of the two fiber lengths can be represented as

$$\frac{1}{2}E_0 e^{i(knz_s - \pi)}, \tag{5}$$

where z_s is the total physical length of fiber the light traversed from the laser, through the coupler, out to the mirror, and back through the coupler to the detector. The phase inverse of the electric field ($e^{-i\pi}$) is included to account for electric field reflection at a high-index mirror. The factor of two fractional reduction in eq. 5 results from two passes of a 50/50 coupler, with each pass reducing electric field amplitude via $1/\sqrt{2}$ scaling. The electric field arriving at the detector as a result of traversing the longer length of fiber can be represented as

$$\frac{1}{2}E_0 e^{i(kn(z_s+2l) - \pi)}, \tag{6}$$

where l is the difference in physical length between the two reflective legs of the interferometer arrangement. The total electric field arriving at the detector is then

$$E_{det} = \frac{1}{2}E_0(e^{i(knz_s - \pi)} + e^{i(kn(z_s+2l) - \pi)}). \tag{7}$$

As shown in Appendix B.1, following the conversion of electric field to detected power as in eq. 4 yields

$$P_{det} \propto \frac{1}{2}E_0^2(1 + \cos(2knl)). \tag{8}$$

The component of interest in the detected power of eq. 8 is the cosine term. The sinusoidal component provides for interferometer fringing based on modulating wavenumber and/or interferometer length. Because an OFDR is a wavelength-swept system, it is the wavenumber dependence that is of interest here. Fringe spacing of the interferometer, k_Δ, in the wavenumber domain is determined by

$$\begin{aligned} 2k_1 nl - 2k_0 nl &= 2\pi \\ k_\Delta = k_1 - k_0 &= \frac{\pi}{nl}. \end{aligned} \tag{9}$$

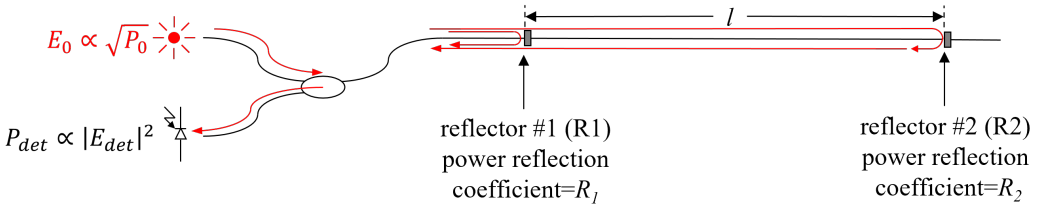

Figure 2. Single-leg in-fiber Michelson interferometer.

An alternative single-leg in-fiber Michelson interferometer is shown in figure 2. In this configuration, the interferometer length l is formed in a single fiber using in-line partial reflectors with unique power reflection coefficients of R_1 and R_2. The electric field returning to the photodetector from R1 is similar to the expression of eq. 5; however, there is now the power reflection coefficient R_1 included:

$$\frac{1}{2}\sqrt{R_1}E_0 e^{i(knz_s-\pi)}. \tag{10}$$

The power reflection coefficient is under the radical in eq. 10 because the power reflection coefficient is the square of electric field reflection coefficient. In this paper, the reflectivity of *optical power* is explicitly referred to as power reflectivity while the reflectivity of *electric field* is simply referred to as reflectivity (no specifier). In eq. 10, z_s is still the total path length from the laser, through the coupler, reflected from R1, and back through the coupler to the detector. Determining the electric field at the detector as a result of the R2 reflection is similar to the determination of eq. 6 with additional inclusions to account for losses due to passing through R1 twice and reflecting from R2 with power reflection coefficient R_2:

$$\frac{1}{2}(1-R_1)\sqrt{R_2}E_0 e^{i(kn(z_s+2l)-\pi)}. \tag{11}$$

If only single-pass propagation is considered (omitting multiple reflections between the two mirrors), the resulting electric field at the detector is the total of the two reflected fields:

$$E_{det} = \frac{1}{2}E_0(\sqrt{R_1}e^{i(knz_s-\pi)} + (1-R_1)\sqrt{R_2}e^{i(kn(z_s+2l)-\pi)}). \tag{12}$$

Just as in eq. 8, the power at the detector is proportional to the conjugate square of the electric field. Omitting reduction steps, the resulting power is given by

$$P_{det} \propto \frac{1}{4}E_0^2(R_1 + (1-R_1)^2R_2 + 2(1-R_1)\sqrt{R_1R_2}\cos(2knl)). \tag{13}$$

As with the previous configuration, the resulting signal at the detector contains a term that has sinusoidal dependence on wavenumber and interferometer length. If the second reflector, R2, of the single leg interferometer is simply a cleaved fiber end in air, there is no phase inversion of the electric field at the back reflection. The resulting electric filed at the detector is then

$$E_{det} = \frac{1}{2}E_0(\sqrt{R_1}e^{i(knz_s-\pi)} + (1-R_1)\sqrt{R_2}e^{ikn(z_s+2l)}) \tag{14}$$

and the corresponding power at the detector is found to be

$$P_{det} \propto \frac{1}{4}E_0^2(R_1 + (1-R_1)^2R_2 + 2(1-R_1)\sqrt{R_1R_2}\cos(2knl + \pi)). \qquad (15)$$

Comparison of eq. 15 to eq. 13 shows that the inclusion or exclusion of a phase inversion at a reflection affects only the phase of the oscillatory signal of the interferometer. Because the reflection phase inversion only affects the phase of the signal of interest, electric field phase inversion at reflections will not be included in signal derivations for the remainder of the text. Additionally, of note in the signal representations of the two different in-fiber Michelson interferometer configurations is the absence of the length term z_s. This shows that the outputs of the configurations are unaffected by the traversed distance from the source laser, to the first mirror, and back to the detector. Because of the absence of dependence on the location of the first mirror/reflector, the length term z_s is omitted from subsequent signal analysis. Of interest in this discussion is only the length difference between the mirrors, which determines the interferometer length.

Simple dual-Michelson OFDR fiber network

An OFDR fiber network, in its simplest form, is simply two in-fiber Michelson interferometers that share a common source. One of the interferometers is configured as a *sensing leg* and another configured as a *reference leg*. The sensing leg contains the FBG sensor of interest, configured as the second reflector in a single-leg in-fiber Michelson interferometer, and the reference leg consists of a dual-leg in-fiber Michelson interferometer. To maximumize interference in the reference leg, regardless of polarization changes (birefringence) along the reference fiber, Farady rotator mirrors are typically utilized for mirrors M1 and M2. A diagram of the network is shown in figure 3.

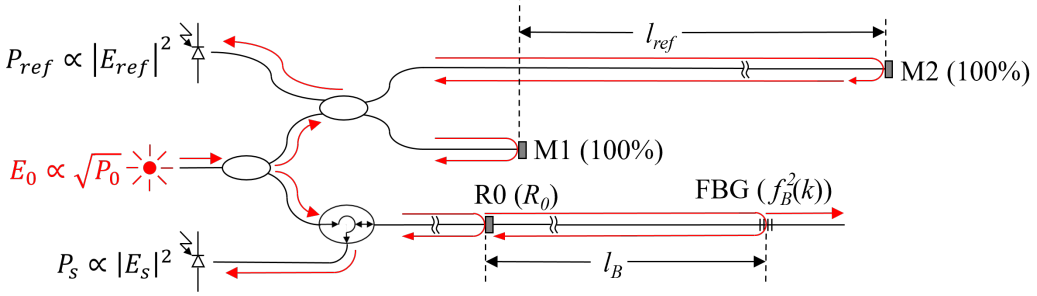

Figure 3. Simple dual-Michelson OFDR fiber network.

In the network of figure 3, a coupler splits the source power between the reference leg and the sensing leg. A circulator replaces the coupler in the sensing leg to provide isolation of the sensing leg from the rest of the network and subsequently eliminates the 6 dB power reduction associated with the use of a 50/50 coupler (3 dB loss in each direction). With the reference interferometer length now specified as l_{ref} and the addition of an extra coupler reducing power by 3 dB, the power P_{ref} at the

reference leg detector is similar to the result in eq. 8:

$$P_{ref} \propto \frac{1}{4} E_0^2 (1 + \cos(2knl_{ref})). \tag{16}$$

The fringe spacing of the reference interferometer in the OFDR network is then

$$k_\Delta = \frac{\pi}{nl_{ref}}. \tag{17}$$

The power P_s at the sensing leg detector is expressed similarly to eq. 13, however modified with the first power reflection coefficient represented as R_0 of partial reflector R0, the second power reflection coefficient represented as the square of an FBG reflection function of wavenumber ($f_B^2(k)$), and the interferometer length set by distance l_B between partial reflector R0 and the center of the FBG:

$$P_s \propto \frac{1}{2} E_0^2 \left(R_0 + (1 - R_0)^2 f_B^2(k) + 2 (1 - R_0) f_B(k) \sqrt{R_0} \cos(2knl_B) \right). \tag{18}$$

Similar to eq. 13, the resulting signal at the detector of the sensing leg contains a term that has sinusoidal dependence on wavenumber and interferometer length l_B. For a low-reflectivity FBG, the effects of a second pass, or second order, reflection caused by the partial reflector R0 reflecting power back into the sensing fiber where it again reflects at the FBG, and partially transmits through R0 and back to the sensing leg detector, is insignificant in comparison to the first order interference and is therefore ignored in this analysis. For consistency with the previously specified relationship between *power reflectivity* and *reflectivity* with no specifier, the FBG power reflection function $f_B^2(k)$ is simply the square of the pure-real FBG reflection function $f_B(k)$, also known as the *reflection spectrum* or *spectral response*. The electric field phase inversion associated with the reflection function is omitted – consistent with the treatment of simple mirrors in this paper.

Dual-Michelson OFDR fiber network with multiple FBG sensors

The typical OFDR sensing scenario in which M FBG sensors are inscribed on a single sensing fiber is shown in figure 4.

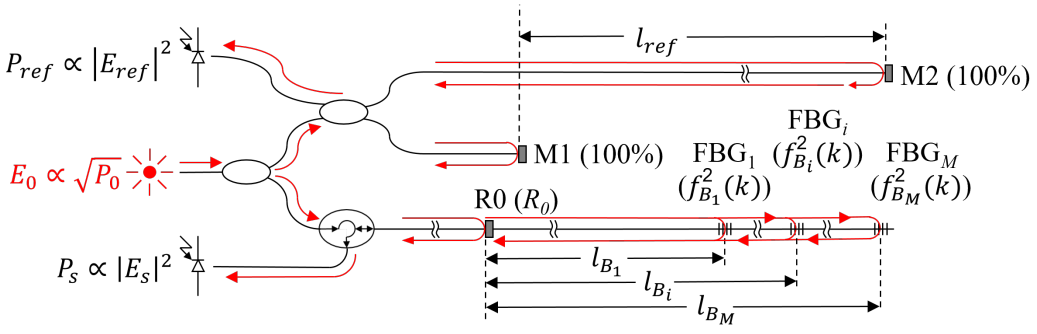

Figure 4. Dual-Michelson OFDR fiber network with multiple FBG sensors in the sensing fiber.

Because the recombining of the electric fields in the sensing fiber occur at the location of R0, the partial reflector R0 is often referred to as the *reference* reflector and sets the $z = 0$ location in, or distance along, the sensing fiber. Positive z values correspond to locations in, or distance along, the sensing fiber in a direction away from R0. Using the location of the reference reflector as $z = 0$ in the sensing leg of the network, the E-field reflected at R0 is represented as

$$\frac{1}{\sqrt{2}}\sqrt{R_0}E_0 \tag{19}$$

and the electric field propagating out to the FBG cluster is

$$\frac{1}{\sqrt{2}}\sqrt{1-R_0}E_0 e^{iknz}. \tag{20}$$

The electric field propagating out to FBG number m and reflecting back through the reference mirror is given by

$$\frac{1}{\sqrt{2}}\left(1-R_0\right)E_0 f_{B_m}(k)e^{ik2nl_{B_m}}. \tag{21}$$

Including every FBG in the sensing fiber and ignoring second pass, or second order, interference as was done in the single FBG analysis leads to the total electric field E_s at the sensing leg detector being

$$E_s = \frac{1}{\sqrt{2}}E_0\left(\sqrt{R_0} + (1-R_0)\sum_{m=1}^{M} f_{B_m}(k)e^{ik2nl_{B_m}}\right). \tag{22}$$

As pointed out earlier, the relative (not absolute) amplitudes of signals are of importance in the analysis presented in this paper, so dropping the common multiplier $E_0/\sqrt{2}$ is acceptable and useful to simplify eq. 22 before determining a proportional corresponding power at the sensing detector. As shown in Appendix B.2, the corresponding power representation P_s at the sensing leg detector is

$$P_s \propto R_0 + 2\sqrt{R_0}(1-R_0)\sum_{m=1}^{M} f_{B_m}(k)\cos\left(2knl_{B_m}\right) + (1-R_0)^2\sum_{m=1}^{M} f_{B_m}^2(k) + 2(1-R_0)^2\sum_{m=1}^{M-1}\sum_{j=m+1}^{M} f_{B_m}(k)f_{B_j}(k)\cos\left(2kn(l_{B_j}-l_{B_m})\right). \tag{23}$$

3 Signal Processing

The following uses a simulation of OFDR signals to illustrate the interrogation and measurement of a sensing fiber with 15 FBGs. The basic steps are summarized as (1) sample the raw data, (2) Fourier transform the raw data to the spatial set, (3) Inverse Fourier transform the spatial data of each FBG to individual FBG spectral sets, and (4) determine the Bragg wavelength of each FBG.

FBG reflection function

An important component of the signal analysis is to consider a realistic model for the reflection function $f_B(k)$. The particular FBGs typically used as sensors in OFDR applications are very low in reflectivity. For example, the FBGs utilized in the demonstration measurement of Section 5 have approximately 0.03% reflectivity. They are also typically no longer than 10 mm and can be as short as is needed for the application, although less than two or three mm is not commonly utilized in practical application. While much attention is given in literature to modeling FBG modulation structures and their resultant reflection functions, the low-reflectivity type of FBG used in the configuration described here exhibits a spectral response that is well approximated by simply Fourier transforming the envelope function of the periodic index modulation which forms an FBG [10]. For this discussion, the index modulation amplitude and spacing are considered constant over the length of the FBG (constant envelope and zero chirp), which results in a reflection spectrum approximated as a pure-real sinc function vs. wavenumber. Using the derivation detailed in Appendix C.2, the FBG reflection function will be approximated by

$$f_B(k) \approx \sqrt{R_B}\,\mathrm{sinc}\left(\frac{2nL_B(k-k_B)}{2\pi}\right), \tag{24}$$

where $\sqrt{R_B}$ is the the FBG peak reflection coefficient, L_B is the physical length of the FBG, and k_B is the Bragg wavenumber of the FBG. As was present in previous equations concerning lengths of fiber in the OFDR arrangement, the $2n$ term present in eq. 24 scales the apparent length of the FBG to account for the out-and-back propagation of light through effective index n. The Bragg wavenumber k_B is related to the resonant Bragg wavelength λ_B by

$$k_B = \frac{2\pi}{\lambda_B}. \tag{25}$$

Sampling the raw data set

The signals of interest in the sensing leg signal of eq. 23 are the grating[1] reflection functions $f_{B_m}(k)$. Because $f_{B_m}(k)$ appear as amplitude modulations of sinusoidal functions, Fourier transform analysis is a simple method of decoupling grating responses. However, such analysis requires that the sampled sensing leg signal have a linear basis. This is accomplished using the detection and sampling electronics of figure 5.

[1]For the purpose of readability through the remaining text, the informal term "grating" will often be used in place of the more formal terms "fiber Bragg grating" and "FBG".

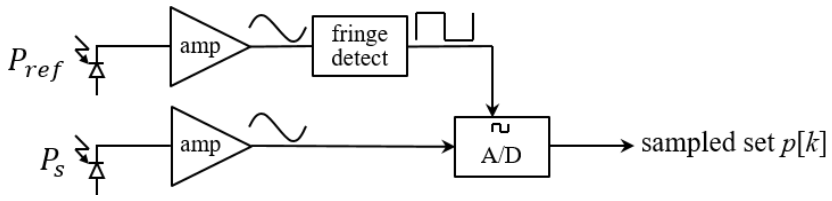

Figure 5. OFDR detection and sampling electronics.

The derivation of the two signals P_{ref} and P_s at the detectors of the dual-Michelson fiber network typically utilized in an OFDR system was explored in Section 2. In the arrangement of figure 5, the sinusoidal term of the reference leg signal P_{ref} is converted to a square wave with a period in the basis of wavenumber as according to eq. 17: $k_\Delta = \pi/nl_{ref}$. The fringe-based square wave is then used to clock the sampling of the sensing leg signal P_s via an A/D converter when the source laser is swept in wavenumber. The sampled set, or the *raw data*, is a discretized representation of eq. 23:

$$p\,[k] \triangleq R_0 + 2\sqrt{R_0}(1-R_0)\sum_{m=1}^{M} f_{B_m}(k)\cos\left(2knl_{B_m}\right) + (1-R_0)^2\sum_{m=1}^{M} f_{B_m}^2(k) + 2(1-R_0)^2\sum_{m=1}^{M-1}\sum_{j=m+1}^{M} f_{B_m}(k)f_{B_j}(k)\cos\left(2kn(l_{B_j}-l_{B_m})\right) \quad (26)$$

for

$$k \triangleq \{k_0 + i * k_\Delta | i \in \mathbb{N}_0, i \leq N-1\}, \quad (27)$$

where k is the linear basis, k_0 is the start wavenumber of the basis, k_Δ is the basis interval, and N is the number of data points recorded. To ease analysis, detector/amplifier transimpedance gain factors and transfer functions such as high-pass filters are not included in eq. 26. While such factors can be of importance in more complex OFDR systems and applications, they have little effect on the basic implementation of an OFDR presented here. Substituting the approximation of an FBG reflection function as found in eq. 24 for each $f_{B_m}(k)$ in eq. 26 and assuming the gratings have identical maximum reflection R_B and length L_B leads to:

$$p\,[k] \triangleq R_0 + 2\sqrt{R_0 R_B}(1-R_0)\sum_{m=1}^{M}\operatorname{sinc}\left(\frac{2nL_B(k-k_{B_m})}{2\pi}\right)\cos\left(2knl_{B_m}\right) + (1-R_0)^2 R_B\sum_{m=1}^{M}\operatorname{sinc}^2\left(\frac{2nL_B(k-k_{B_m})}{2\pi}\right) + 2(1-R_0)^2 R_B\sum_{m=1}^{M-1}\sum_{j=m+1}^{M}\operatorname{sinc}\left(\frac{2nL_B(k-k_{B_m})}{2\pi}\right)\operatorname{sinc}\left(\frac{2nL_B(k-k_{B_j})}{2\pi}\right)\cos\left(2kn(l_{B_j}-l_{B_m})\right) \quad (28)$$

The assumptions – that maximum reflectivity and length are equal from grating to grating along a sensing fiber – are consistent with common practical implementation of an OFDR measurement system [11]. Although the maximum reflectivity of individual gratings can be affected by production discrepancies and environmental factors, the reflectivity variance does not affect the analysis detailed here.

Plotted in figure 6 is simulated raw data using eq. 28 for 15 FBGs ($M = 15$)with Bragg wavelengths randomly generated betwen $1553 \pm .25$ nm ($\lambda_{1:15}$), distributed from 7 to 7.14 m at 1 cm spacing ($l_{B_{1:15}} = \{7.00, 7.01, ..., 7.14\}$), FBG length 9 mm ($L_B = .009$), and maximum reflectivity 0.1% ($R_B = 0.001$). The OFDR fiber network and scan parameters used in the simulation are a reference length of 20 m ($l_{ref} = 20$), effective index of refraction 1.4682 ($n = 1.4682$), broadband in-line reflection coefficient of 30% ($R_0 = 0.3$), laser sweep low wavelength of 1545 nm ($k_0 = 2\pi/1545 \times 10^{-9}$), and raw data set size of 524288 ($N = 524288$). The data of figure 6 are not digitized; i.e., the bit resolution of an A/D converter is not implemented in the raw data simulation.

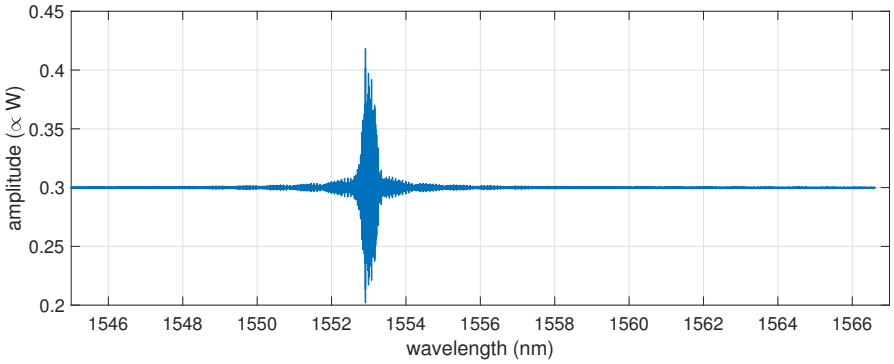

Figure 6. Simulated raw data set: power vs. wavelength.

The basis interval k_Δ of the simulated raw data is calculated using eq. 17 to be 0.107 m^{-1} and the basis of the simulated raw data set is accordingly:

$$k \triangleq \left(2\pi/\left(1545 \times 10^{-9}\right) - i * 0.107\right) | i \in \mathbb{N}_0, i \leq 524287. \tag{29}$$

In this simulation, the sampling of the sensing fiber sensor is assumed to occur during an increasing wavelength sweep – thus the negative iteration of the basis in wavenumber. Although the raw data is sampled such that it is linear in *wavenumber*, it is common to characterize the sampling of raw data as *versus wavelength*. Accordingly, the wavenumber basis of eq. 29 is converted to wavelength to set the x-axis of fig. 6. Additionally, because the *resolution* of an OFDR system is usually specified in wavelength, the equivalent *wavelength resolution* at wavelength λ_i of the sampled data can be found using

$$\frac{2\pi}{\left(\frac{2\pi}{\lambda_i}\right) - k_\Delta} - \lambda_i. \tag{30}$$

At the start of the simulated wavelength sweep (1545 nm), the equivalent wavelength resolution of the raw data is 40.7 fm and at the end of the sweep (1556.6 nm) the equivalent wavelength resolution is 41.8 fm.

The spatial set

Before proceeding with the analysis of the signal processing of the sampled raw data set and beyond, it is important to note that in this discussion, the term "Fourier transform" refers to the application of Fourier transform theory in a *general* sense; precise amplitude scaling and representations customarily applied to discrete implementations are not necessarily included in the signal processing analysis. Because the raw data set is sampled vs. wavenumber with the basis unit being radians/meter, the Fourier transform result has the basis unit of meters/radian, represented as "z" in this analysis. The location of the partial reflector R0 corresponds to $z = 0$ and any non-zero z corresponds to a distance from R0 to a location in the sensing fiber. Fourier transforming the raw data produces a result that is often described as the *spatial* set existing in the *spatial* domain, due to the resulting basis unit being meters/radian. The spatial set $P[z]$ is formed by

$$P[z] = \mathcal{F}\{p[k]\} \tag{31}$$

and the spatial set basis interval $\tilde{z}_\Delta$ determined by

$$\tilde{z}_\Delta = \frac{1}{k_\Delta N} \tag{32}$$

with the corresponding units of meter/radians. The spatial set of the simulated raw data, i.e., the Fourier transform (magnitude of the complex result) of the simulated raw data, is shown in figure 7.

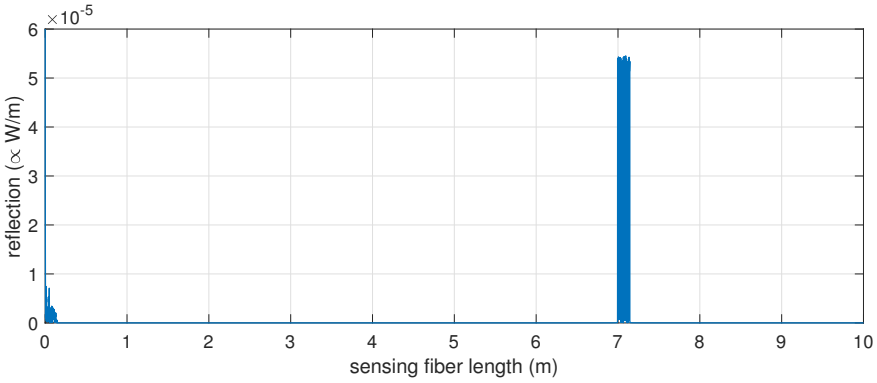

Figure 7. Fourier transform of the simulated raw data set yields the simulated spatial set: reflection (magnitude of complex spatial set) vs. sensing fiber length. Only the front half of the spatial set is plotted.

To comprehend the data of the spatial set and to properly relate the information of the spatial set to real-world length along the sensing fiber, the spatial set basis

determined by eq. 32 is scaled by multiplying by 2π radians/meter and dividing by $2n$ to account for the out-and-back propagation of light through the fiber with index of refraction n. The real-world basis interval z_Δ of the spatial data is thus

$$z_\Delta = \frac{1}{k_\Delta N} \times \frac{2\pi}{2n} = \frac{l_{ref}}{N}, \tag{33}$$

and the x-axis of the spatial plot is defined by

$$z \triangleq \{i * z_\Delta | i \in \mathbb{N}_0, i \leq N-1\}. \tag{34}$$

In this example, z_Δ, often referred to as the *spatial resolution*, is 38.2 μm. Because the raw data is pure-real, the second half of the spatial set is simply a mirror of the first half. Therefore, in typical applications of the methodology, only the first half of the spatial set is considered.

By linearity, the Fourier transform of the raw data defined in eq. 28 can be explored one term at a time. The partial reflector term R_0 is the result of a non-varying reflection from the inline broadband reflector. It Fourier transforms to a delta function at distance zero ($R_0\delta(0)$).

The second term is

$$2\sqrt{R_0 R_B}(1-R_0) \sum_{m=1}^{M} \text{sinc}\left(\frac{2nL_B(k-k_{B_m})}{2\pi}\right) \cos(2knl_{B_m}), \tag{35}$$

which, as detailed in Appendix C.4, Fourier transforms to

$$\pi\,(1-R_0)\,\sqrt{R_B R_0} \sum_{m=1}^{M} e^{-ik_{B_m}(z-2nl_{B_m})}\,\text{rect}\left(\frac{z-2nl_{B_m}}{2nL_B}\right). \tag{36}$$

Equation 35 contains the functions of interest $f_{B_m}(k)$ acting as amplitude modulators of sinusoids (cosine) whose frequencies are set directly and uniquely by l_{B_m}. This term is the result of grating reflections interfering with the inline broadband reflector. The rectangle functions in eq. 36 are non-zero at the unique locations of the gratings along the sensing fiber and the exponential term accompanying each rectangle function uniquely carries the Bragg wavenumber information in the complex phase of the Fourier transform result. The reflections (magnitude of the complex spatial set) of the 15 gratings in the simulated spatial set are shown in figure 8.

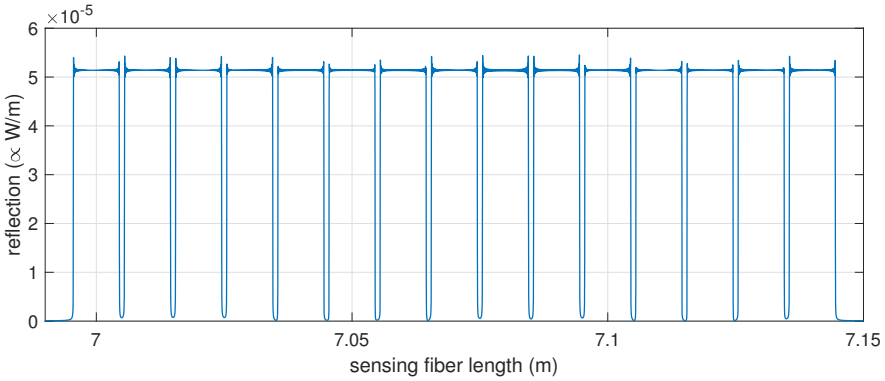

Figure 8. Reflections from distributed FBGs in the simulated spatial data set: reflection (magnitude of complex spatial set) vs. sensing fiber length.

The third term of the raw data in eq. 28 is

$$(1-R_0)^2 R_B \sum_{m=1}^{M} \operatorname{sinc}^2\left(\frac{2nL_B(k-k_{B_m})}{2\pi}\right). \tag{37}$$

As detailed in Appendix C.3, this term Fourier transforms to

$$\frac{\sqrt{2\pi}(1-R_0)^2 R_B}{2nL_B} \sum_{m=1}^{M} e^{-ik_{B_m}z} \operatorname{tri}\left(\frac{z}{2nL_B}\right). \tag{38}$$

This term represents the reflections from all of the gratings directly arriving at the sensing leg detector. In the result of eq. 38, each grating has a triangle function that is representative of it interfering with itself, thus creating an auto-convolution of its reflection (a rectangle function) in the spatial domain. The magnitude of the Fourier transform of the third term from the raw data simulation is plotted in figure 9.

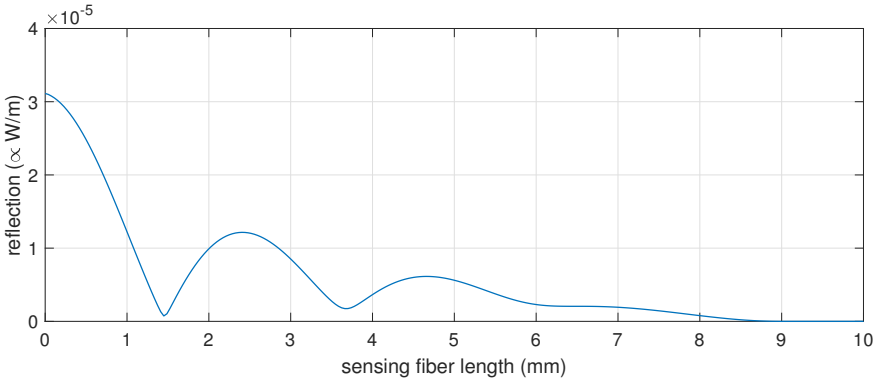

Figure 9. FBG auto-convolution result in the simulated spatial data set: reflection (magnitude of complex spatial set) vs. sensing fiber length.

The result of summing the terms in the spatial domain is greatly affected by the differing grating wavenumbers k_{B_m} via the relative phase of each triangle function. However, the non-zero contribution is spatially limited to the grating length L_B, which is 9 mm in the simulated sensing scenario.

The fourth term of the raw data in eq. 28 is a double summation of the interaction between all of the gratings on the sensing fiber:

$$2(1-R_0)^2 R_B \operatorname{sinc}\left(\frac{2nL_B(k-k_{B_m})}{2\pi}\right) \operatorname{sinc}\left(\frac{2nL_B(k-k_{B_j})}{2\pi}\right) \cos\left(2kn(l_{B_j}-l_{B_m})\right). \tag{39}$$

Equation 39 shows how each grating forms an interferometer with all of the other gratings. The interferometer lengths are set by the spacing of the gratings $(l_{B_j}-l_{B_m})$ and the level of interaction between gratings depends on the separation between k_{B_m} and k_{B_j}. Appendix C.5 details the derivation of the Fourier transform of this double-sum term to be expressed as

$$\frac{R_B(1-R_0)^2}{2n^2L_B^2} \sum_{m=1}^{M-1} \sum_{j=m+1}^{M} G_{m,j}(z). \tag{40}$$

$G_{m,j}(z)$ is a grating to grating coss-convolution function, derived in Appendix C.5, that represents the many possible results of grating to grating interaction and is non-zero only in the interval $z = 2n(l_{B_j}-l_{B_m}) \pm 2nL_B$. It is explicitly defined as

$$G_{m,j}(z) = \begin{cases} \frac{e^{-ik_{B_m}z}(e^{-i(z+nL_B)k_{B_\Delta}} - e^{-i(-nL_B)k_{B_\Delta}})}{-ik_{B_\Delta}} & \text{if } -2nL_B \le z-2n(l_{B_j}-l_{B_m}) \le 0 \\ \frac{e^{-ik_{B_m}z}(e^{-i(nL_B)k_{B_\Delta}} - e^{-i(z-nL_B)k_{B_\Delta}})}{-ik_{B_\Delta}} & \text{if } 0 < z-2n(l_{B_j}-l_{B_m}) \le 2nL_B \\ 0 & \text{otherwise} \end{cases} \tag{41}$$

where $k_{B_\Delta} = k_{B_j} - k_{B_m}$. This result is similar to the grating auto-convolution result in that the Fourier transform of the two sinc functions and the sinusoidal (cosine) of eq. 39 is found via convolution of two rectangle functions based on grating length and a delta function based on the distance between grating pairs. The differing grating wavenumbers k_{B_m} and k_{B_j} between grating pairs affects the convolution of the paired rectangle functions via complex phase differences between the two. This work will not explore the explicit solution of $G_{m,j}(z)$ beyond the definition that is non-zero only in the interval $z = 2n(l_{B_j}-l_{B_m}) \pm 2nL_B$. The magnitude of the Fourier transform of the fourth term from the raw data simulation is plotted in figure 10.

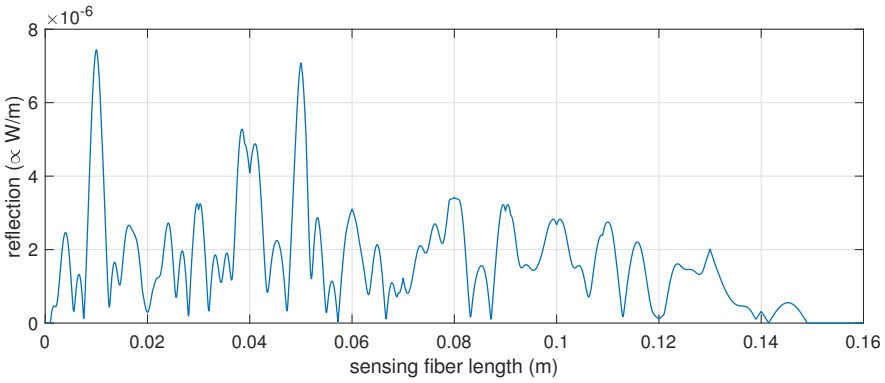

Figure 10. FBG cross-convolution result in the simulated spatial data set: reflection (magnitude of complex spatial set) vs. sensing fiber length.

The magnitude of the cross-convolution result goes to zero at .149 m, which corresponds to the maximum distance between two gratings (14 cm) plus the length of the gratings (9 mm). Note that the magnitude of the cross-convolution terms is only 1 order of magnitude below that of the grating reflection magnitude. For this reason, when OFDR is used to interrogate hundreds of gratings, it is best practice to place the first grating at a distance from the reference reflector that is at minimum the largest distance between two grating pairs. For example, if 300 gratings are in a sensing fiber and distributed 1 cm center-to-center, the largest spatial separation between two grating pairs is 299 cm. Any gratings within 299 cm of the reference reflector could experience interference from the cross-convolution terms, introducing degradation of measurement accuracy.

FBG reflection spectra and Bragg wavelength determination

The spectrum of an individual grating is found by inverse Fourier transforming the complex spatial data of the grating of interest. The spatial reflection data, separated into magnitude and unwrapped phase, for the first grating in the simulated sensing fiber are plotted in figure 11.

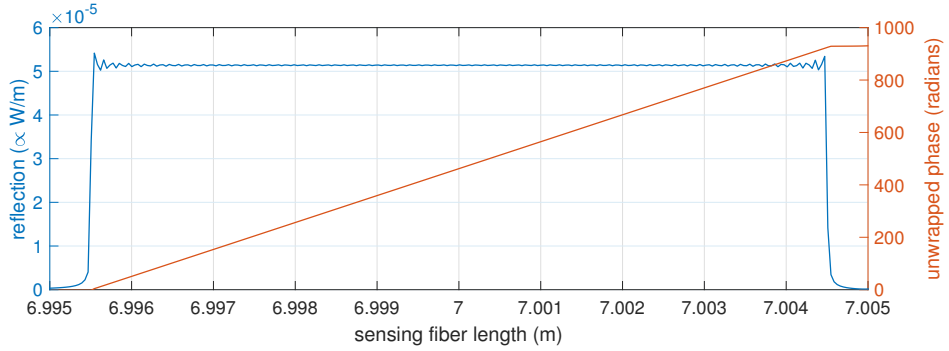

Figure 11. Reflection of the first FBG in the simulated spatial data set: reflection (magnitude of complex spatial set) vs. sensing fiber length.

The complex spatial data of the grating shown in figure 11 inverse Fourier transforms to the individual reflection spectrum of the grating, the magnitude of which is plotted in figure 12. It is important to note that the inverse Fourier transform operation is not performed on the *magnitude* of the grating spatial data, which is used to form the plot in figure 11 - it is performed on the *complex* spatial data, which, as was shown in eq. 36, carries the Bragg wavenumber information within its phase.

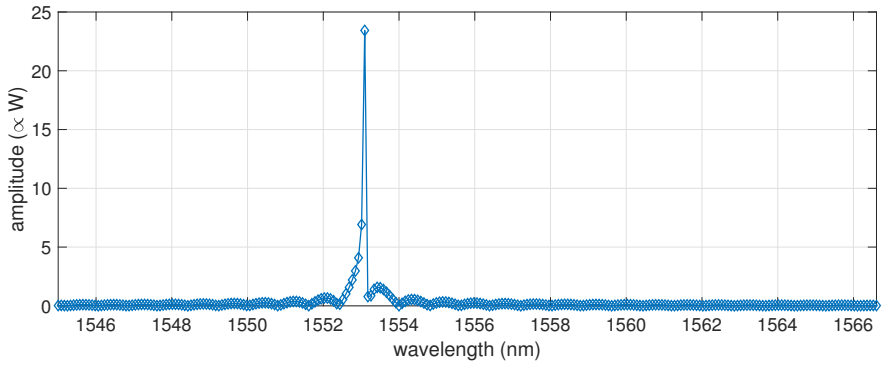

Figure 12. Reflection spectrum of the first FBG in the simulated sensing fiber: power vs. wavelength.

The formal representation of this transformation to the grating *spectral* set $\tilde{p}[\tilde{k}]$ is

$$\tilde{p}[\tilde{k}] = \mathcal{FFT}^{-1}\{P_B[z]\}, \tag{42}$$

where $P_B[z]$ is the set of windowed, or band pass filtered, complex grating spatial data and $\tilde{k}$ is the wavenumber basis of the grating spectral set. As was implemented in plotting raw data in figure 6, the x-axis of figure 12 is converted to wavelength for only for ease of qualitative comprehension. Calculations involving the spectral set should use the wavenumber basis of spectral set. The spectral set basis interval $\tilde{k}_\Delta$ of the spectral set in eq. 42 and the data in figure 12 is determined by

$$\tilde{k}_\Delta = \frac{1}{\tilde{z}_\Delta \tilde{N}} = \frac{k_\Delta N}{\tilde{N}}, \tag{43}$$

where $\tilde{N}$ is the number of data points in the grating spectral set. Of note in the spectral data of figure 12 is the limited number of points (~ 9) that define the grating's reflection band. As discussed in Section 1, the use of an FBG sensor typically involves tracking shifts in the sensor's Bragg wavelength. For this reason, the particular algorithm or method used to calculate the Bragg wavelength from a spectral set such as is shown in figure 12 can have a significant effect on the accuracy of an OFDR FBG measurement. Additionally, processor-intensive algorithms such as correlation or curve-fitting can significantly affect measurement latency. A discussion of the pros and cons of the numerous possible algorithms that may find use in determining the Bragg wavelength is not included in this paper. What is presented here is a commonly-utilized, relatively simple method that makes use of the previously considered approximation of the FBG spectral response as a sinc function.

Zero-padding the windowed complex grating spatial data of figure 11 before the inverse Fourier transform operation results in a reflection spectrum that resembles the expected sinc function and is conducive to simple thresholding and center-of-mass peak detection. Plotted in figure 13 is the reflection spectrum of the first grating after zero padding the complex grating spatial set to $\tilde{N} = 2048$. With the assumption that the Bragg wavelength is the centroid of the singular dominant spectral peak as is seen in figure 13, the spectral points of the dominant peak are isolated via thresholding and then processed via a center-of-mass algorithm to determine the Bragg wavelength.

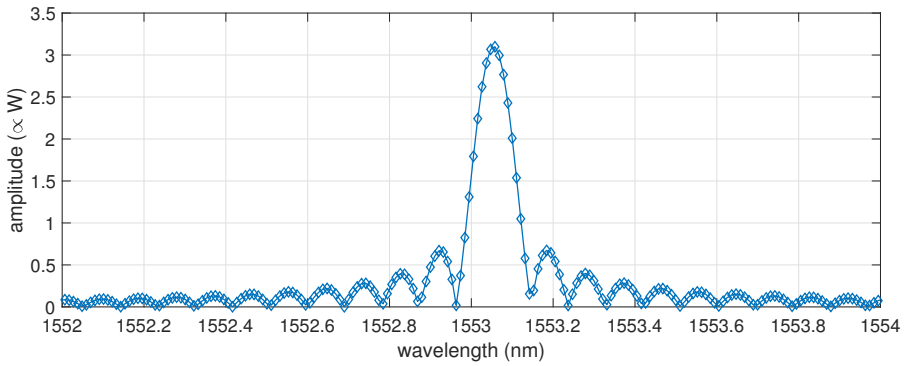

Figure 13. Reflection spectrum of the first FBG in the simulated sensing fiber using the zero-padded spatial set: power vs. wavelength.

A zoomed view of the spectral data at and around the grating reflection peak is shown in figure 14. Also plotted in figure 14 are the points used in the center-of-mass calculation and the associated centroid result. In this simulation, the threshold value was set at 60% of maximum amplitude. Note that the points bounding the thresholded spectral set are linear interpolations based on neighboring points.

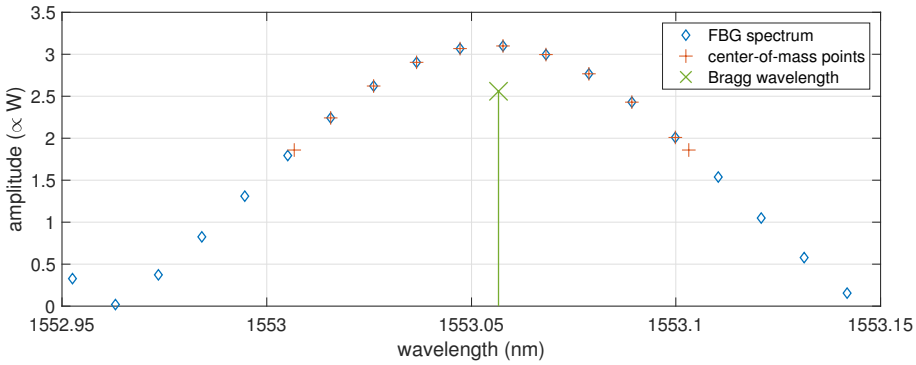

Figure 14. Reflection spectrum data (power vs. wavelength), in the vicinity of the Bragg wavelength, of the first FBG in the simulated sensing fiber with center-of-mass and threshold interpolation points identified.

The center-of-mass algorithm

$$k_B = \frac{\sum_i \tilde{k}_i * |\tilde{p}_i|}{\sum_i |\tilde{p}_i|}, \tag{44}$$

where $\tilde{k}_i$ and $|\tilde{p}_i|$ are the i^{th} wavenumber and reflection magnitude, respectively, of the thresholded spectral set, determines the Bragg wavenumber, and the subsequent conversion to Bragg wavelength follows eq. 25. In the typical implementation of the methodology, completing the interrogation of the sensing fiber requires repeating the steps of: (1) windowing complex FBG spatial data, (2) zero-padding and inverse Fourier transforming the windowed complex FBG spatial data, and (3) calculating the Bragg wavelength from the resulting reflection spectrum, for every FBG sensor of interest.

With the Bragg wavelengths of every FBG sensor determined, the next interrogation of the sensing fiber is initiated with a new sweep of laser wavelength, followed by all of the signal processing steps. As discussed in Section 1, how the Bragg wavelength measurements are utilized depends on the particular application of FBG sensing. In Section 4, the necessary components to assemble an OFDR system are discussed, followed by an example of using FBG sensors to measure surface strain of an aluminum dog bone sample detailed in Section 5.

4 System Primary Components and Requirements

A block diagram of a basic OFDR system is shown in figure 15. In the most basic

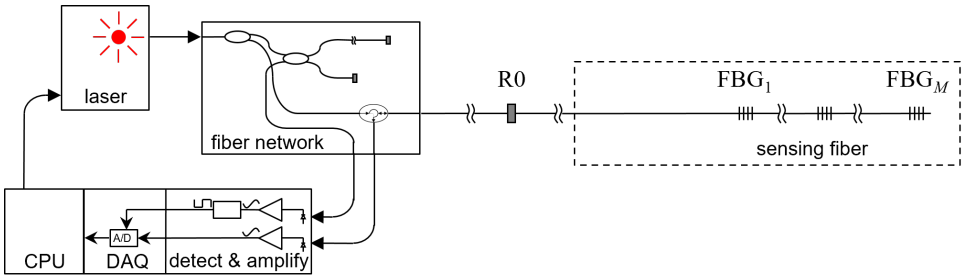

Figure 15. OFDR system block diagram.

configuration, a central processing unit (CPU) controls the laser, stores data, and provides for digital signal processing (DSP). A fiber network distributes the laser output to the internal reference interferometer and the external sensing fiber, and directs optical output of the reference interferometer and the optical reflections of the sensing fiber to the detection/amplification electronics. A data acquisition (DAQ) module performs A/D sampling of the sensing fiber signal and provides the sampled data to the CPU.

Source laser

At the heart of an OFDR is a high spatial-coherence (narrow linewidth), swept wavelength, single longitudinal mode laser providing excitation light for interferometry that occurs both inside the system and in the sensing fiber. The minimum coherence length requirement is governed by the longest expected propagation length for a given application. In a lab setting, this longest length will most likely be twice the length of the OFDR's internal interferometer plus an extra meter to account for system-internal fiber routing, while in a field application, in which the interrogation system and the sensing fiber may be considerably separated (100s of meters), the longest length will be twice the total length of connecting fiber and sensing fiber plus some minimal length ($\sim$ 1 m) to account for system-internal fiber routing. The wavelength sweeping operation must be smooth and monotonic to give smooth interference and ease the acquisition of data during the sweep. Linear sweeping of the laser wavelength vs. time is not required; however, a highly variable sweep rate should be avoided to simplify data acquisition. A monotonic sweep function eliminates the need for extra processing and wavelength tracking, thus simplifying data acquisition.

Fiber and connectors

While a typical OFDR will rely solely on single mode (SM) fiber, some sections of the OFDR network may include the use of polarization maintaining (PM) fiber to eliminate low interference conditions due to differing polarization states of the interfering signals. Depending on the application, the sensing fiber may have different characteristics than the system's internal fiber network; however, it will most likely retain the SM characteristic. For example, a bonded FBG strain gauge application requires the use of bend-insensitive sensing fiber to eliminate the loss of light power due to stress-induced micro-bending along the sensing fiber, yet the internal network components of the OFDR will most likely be linked together via the standard, cheaper, communications-grade SM fiber. Any necessary connectors should be angle-polished to avoid stray reflections appearing in the data. Fusion splices are utilized, when practical, to provide for minimum stray reflections and maximum signal transmission.

Sensors

Because an OFDR is used as a distributed sensing solution, the maximum reflectivity of the individual sensor sections of the sensing fiber should be no more than a fraction of a percent, typically. Special applications in which only a limited number of sensors are utilized allow for higher reflectivity coefficients along the sensing fiber; however, it should be noted that such applications are usually more appropriately addressed with alternative FO sensing solutions such as wavelength division multiplexed (WDM) or optical time domain reflectometer (OTDR) technology. Although an OFDR can be configured to monitor multiple characteristics of a given sensor type, including reflection spectrum (both amplitude and profile), transmission spectrum, group delay, and birefringence, as examples, the typical OFDR sensing

configuration is to monitor the reflection spectra of multiple FBGs to provide distributed strain and/or temperature sensing. Therefore, the focus of this paper is the operation of an OFDR coupled to distributed low-reflectivity FBG sensors in a single sensing fiber. As mentioned previously, FBG sensors have found use in sensing a plethora of physical phenomena; however, in the demonstration of the OFDR-FBG sensing methodology presented in this paper, FBG strain sensing will be the application of interest.

Detection electronics

The conversion of optical signals to electrical signals occurs via photodetectors coupled to transimpedance amplifiers with subsequent signal conditioning, such as filtering and amplification, being application specific. Satisfactory detection/amplification electronics are widely available as COTS items and custom electronics are also relatively simple to construct. The primary specification of OFDR conversion/conditioning electronics, when configured as is detailed in this paper, is the minimum upper bandwidth necessary to perform optical signal conversion and amplification. The factors that influence the minimum upper bandwidth are explored in Section 6.

Data acquisition

The purpose of the DAQ hardware in an OFDR is to record the reflected signal from the sensing fiber while the source laser is swept in wavelength, resulting in a raw data set defined as reflection vs. wavenumber, with a linear wavenumber basis. The DAQ of an OFDR configured in the manner presented in this paper primarily consists of an analog-to-digital (A/D) converter capable of external clocking control (non-constant sampling frequency). Because the source laser is not required to be time-linear in its wavenumber tuning, the A/D sampling rate will most likely be variable, and simply setting an A/D clock speed to a specific frequency will not give satisfactory results. The reasons behind this requirement were explained Section 3. Similar to the detection electronics, the primary specification of the A/D unit is the upper bandwidth limit. Multiple available COTS versions of the necessary DAQ hardware exist, and in specialized applications custom DAQ modules may be required.

Processing and control

A central CPU ties together the sweeping of the laser, data acquisition and output, DSP activities, and recording of data and measurement results. The choices of CPU architectures with satisfactory capabilities are many, from general-use desktop configurations to custom built, flight-qualified, miniaturized systems.

5 Measurement Example

The following example uses a simple aluminum dog bone sample to induce strain into surface-bonded FBG sensors which are interrogated by an OFDR to formulate a strain measurement.

Dog bone sample configuration

The layout of the aluminum 6061 dog bone coupon is diagrammed in figure 16.

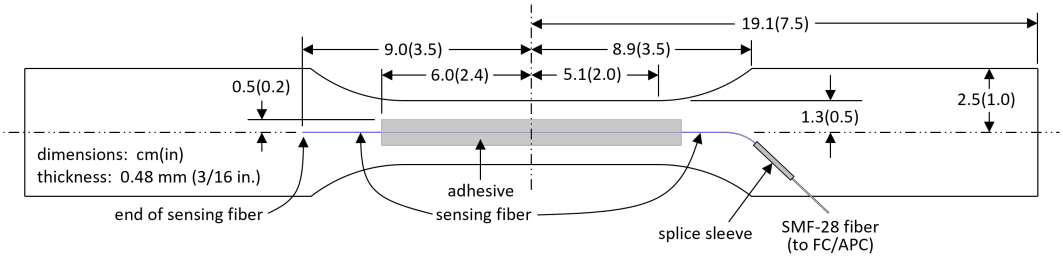

Figure 16. Aluminum coupon layout.

The sensing fiber (FBGS[2] part no. AGF-LBL-1550-125; see Appendix D for specs [11]) contains FBG sensors 9 mm in length, spaced 1 cm center-to-center, and is bonded along the center of the coupon for 12 cm using Henkel Loctite EA 9394 AERO adhesive. To connect to the inline reflector and ultimately to the OFDR interrogator, it is fusion spliced to a standard 900 micron-buffered SMF-28 fiber terminated with an FC/APC connector. A single-axis resistive foil strain gauge (not shown) is bonded to the side opposite of the sensing fiber, centered in width and length, and oriented to measure coupon strain length-wise (in same direction as sensing fiber). An illustration of FBG sensor locations in the sensing fiber is shown in figure 17. There are 20 full-length (9 mm) gratings in the sensing fiber and one

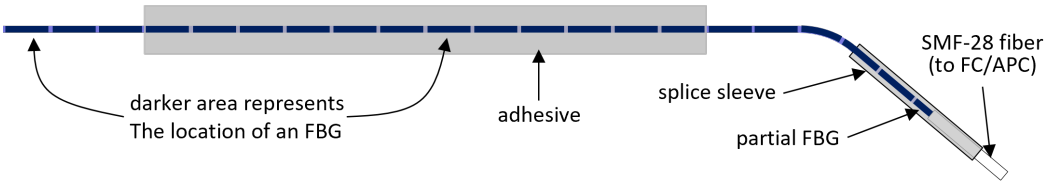

Figure 17. Dog bone coupon sensing fiber diagram. Each FBG sensor is represented by a dark blue section of fiber.

partial-length grating at the fusion splice between the sensing fiber and the SMF-28 fiber leading to the interrogator.

System specifications

The OFDR system used in this example is custom assembled and housed in a National Instruments (NI) PXIE-1065 chassis. The system laser is a New Focus TLM-8700-H-CL. Both the reference leg detector and the sensing leg detector is a Thorlabs model PDB460C. Two National Instruments (NI) DAQ cards, model PXI-6115, control the system timing and raw data sampling. The system control and processing

[2]Specific vendor and manufacturer names are explicitly mentioned only to accurately describe the test hardware. The use of vendor and manufacturer names does not imply an endorsement by the U.S. Government nor does it imply that the specified equipment is the best available.

CPU is an NI PXIE-8135 embedded controller. The fiber network is made of standard communications grade components (SMF-28 equivalent) and contains a 30.182 meter long reference leg of standard SMF-28 fiber with two Faraday rotator mirrors serving as the reference interferometer reflectors. The inline broadband reflector is a titanium-oxide partial reflector (30%) manufactured by AC Photonics. FC/APC connectors are used where necessary (from the laser to the fiber network, for example). The resistive foil gauge is interrogated using an NI cDAQ-9178 chassis with the NI 9236 quarter-bridge strain gage module. An electro-mechanical load frame, the MTS Alliance RT/100 with compression grips, provides tensile exercising of the Al coupon.

Raw data

Shown in figure 18 is a raw data set (524288 points) plotted as return signal vs. wavelength for the Al coupon sensing fiber. The data displayed in figure 18 is mean-zeroed to remove non-oscillatory components of reflection that are of no interest in the measurement. The concentration of substantially increased amplitude at 1550.8 nm is a result of the sensing fiber gratings all having a Bragg wavelength at or near that particular wavelength.

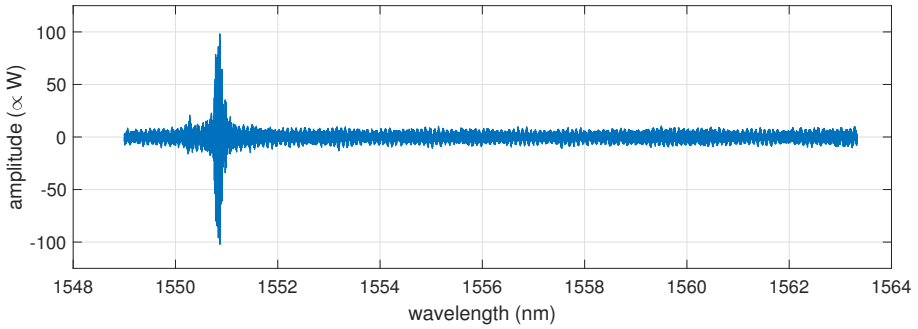

Figure 18. Raw data set: power vs. wavelength..

Zooming in on the wavelength band around 1550.8 nm shows the overlay of multiple FBGs of similar Bragg wavelengths reflecting simultaneously in a single sensing fiber (figure 19).

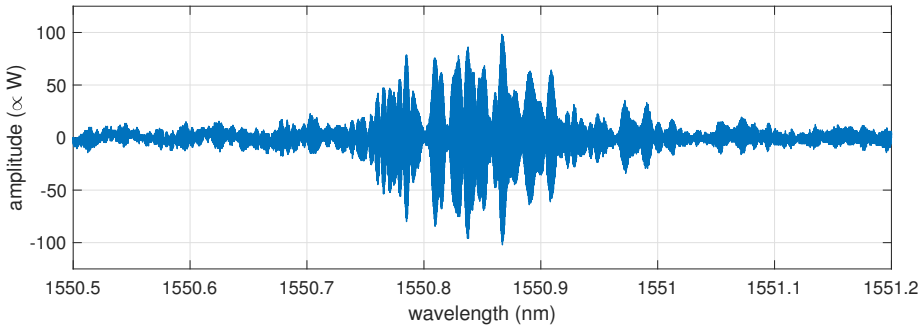

Figure 19. FBG reflection band of raw data set: power vs. wavelength.

With a reference leg length l_{ref} of 30.182 m and an effective index of refraction n of 1.4682, the wavenumber interval k_Δ of the raw data, as specified in eq. 17, is calculated to be .0709 m^{-1}, or approximately 27.1 fm. The start wavelength λ_0 of the sampling is 1549 nm. Using eq. 27 the basis set of the raw data is given by

$$k \triangleq \left(2\pi / \left(1549 \times 10^{-9}\right) - i * 0.0709\right) | i \in \mathbb{N}_0, i \leq 524287. \tag{45}$$

Spatial set

As previously detailed, the raw data of figure 18 is Fourier transformed to give the spatial set; in this example, the commonly utilized FFT is used. The magnitude of the front half of the resulting complex spatial set is plotted in figure 20.

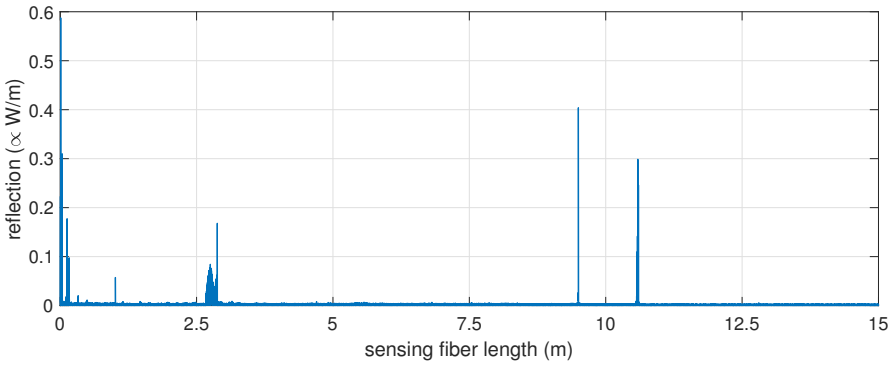

Figure 20. FFT of the raw data set yields the spatial set: reflection (magnitude of complex spatial set) vs. sensing fiber length. Only the front half of the spatial set is plotted.

The gratings in the sensing fiber appear at around 2.8 m. Although the raw data is mean-zeroed, there are still low-frequency components in the spatial set from the auto- and cross-convolution terms, connector discontinuities, and general noise of the system. The sensing fiber in this examples terminates at the end of the grating sensor cluster. Therefore, any significant spatial components located beyond the grating cluster, such as the two strong narrow components near 10 meters, are artifacts of discontinuities and spurious reflections most likely caused by connector imperfections or similar discontinuity-induced reflections in the fiber network. A zoomed in view of the spatial set magnitude at the area of the grating cluster is shown in figure 21.

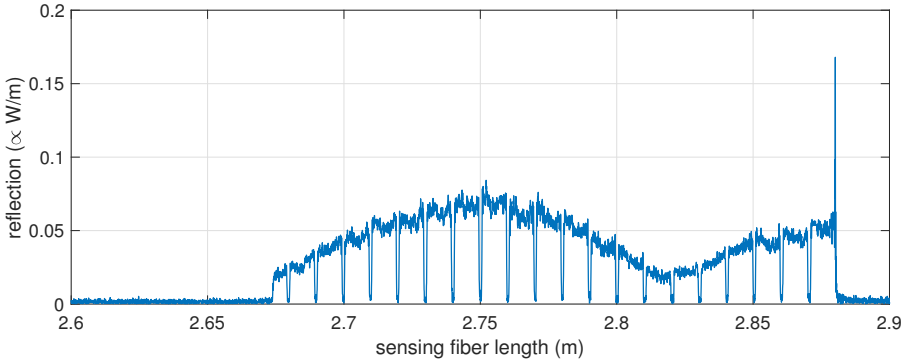

Figure 21. Sensing fiber FBG cluster in the spatial set: reflection (magnitude of complex spatial set) vs. sensing fiber length.

The first grating is cutoff at a fusion splice that connects FBG fiber to a SMF-28 lead cable while the narrow spike at the end of the last grating is the reflection back from the end of the fiber. As specified earlier, the gratings are 9 mm in length with 1 cm center-to-center spacing along the sensing fiber. The non-constant reflection amplitudes of the gratings are due to varying polarization of the light as it propagates through the slightly birefringent fiber. The degree to which the electric field at the reference reflector and the electric field reflected from gratings along the fiber interfere with each other is affected by the relative polarization states of the fields. This phenomenon is addressed in more detail in Section 6.

FBG spectrum

The spatial reflection magnitude and unwrapped phase data for the grating located just after 2.75 m in the sensing fiber are shown in figure 22. This particular grating is within the bonded fiber region with its center located 2.5 cm from the bond line.

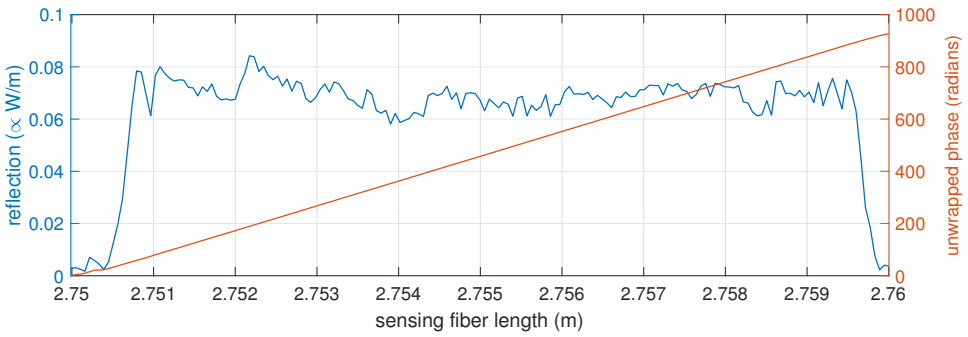

Figure 22. A single FBG reflection in the spatial set: reflection (magnitude of complex spatial set) vs. sensing fiber length.

The complex spatial data of the grating in figure 22 is zero-padded to $\tilde{N} = 2048$

and inverse Fourier transforms via IFFT to the individual reflection spectrum of the grating, the magnitude of which is plotted in figure 23. A zoomed view of the

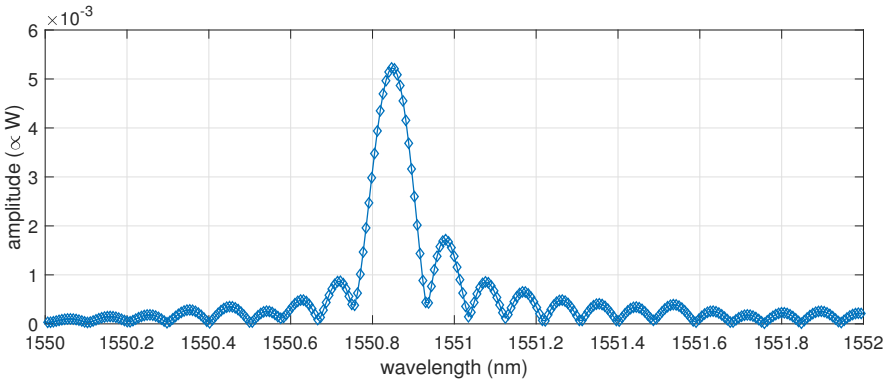

Figure 23. Reflection spectrum of the FBG centered at 2.755 m along the sensing fiber: power vs. wavelength.

spectral data at and around the reflection spectrum peak is shown in figure 24. Also plotted in figure 24 are the points used in the center-of-mass calculation and the associated centroid result. In this example, the threshold value was set at 60% of maximum amplitude. The points bounding the thresholded spectral set are linear interpolations based on neighboring points. Using the center-of-mass calculation of

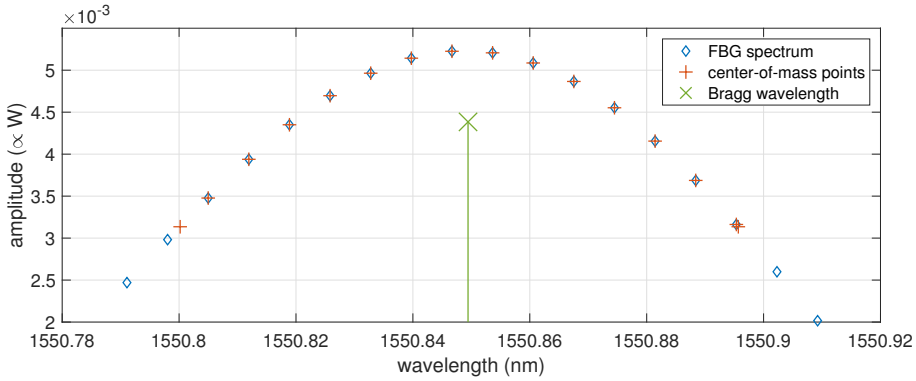

Figure 24. Reflection spectrum data (power vs. wavelength), in the vicinity of the Bragg wavelength, of the FBG centered at 2.755 m along the sensing fiber with center-of-mass and threshold interpolation points identified.

eq. 44, the Bragg wavelength of this grating is determined to be 1550.849 nm.

Strain measurement

In typical application, the measurement of strain in an FBG strain sensor is inferred via the tracking of the Bragg wavelength shift. The dependence of FBG spectral shift on axial strain, for constant temperature, is given by

$$\Delta\lambda_B = \lambda_{B_0}(1 - p_e)\varepsilon, \tag{46}$$

where $\Delta\lambda_B$ is the spectral shift of the Bragg wavelength, λ_{B_0} is the Bragg wavelength at zero strain, p_e is the effective strain-optic constant, and ε is the axial strain within the FBG [12]. The gauge factor of an FBG strain gauge is thus $(1 - p_e)$. Shown in figure 25 are the reflection spectra of the previously explored FBG (the FBG of figure 22) for seven different strain levels, as measured by the resistive foil gauge, in the dog bone sample. Each reflection spectrum is normalized to the maximum value of the zero strain case. Applying the threshold and center-of-mass algorithm to the spectra of figure 25 yields the Bragg wavelength vs. strain plot of figure 26.

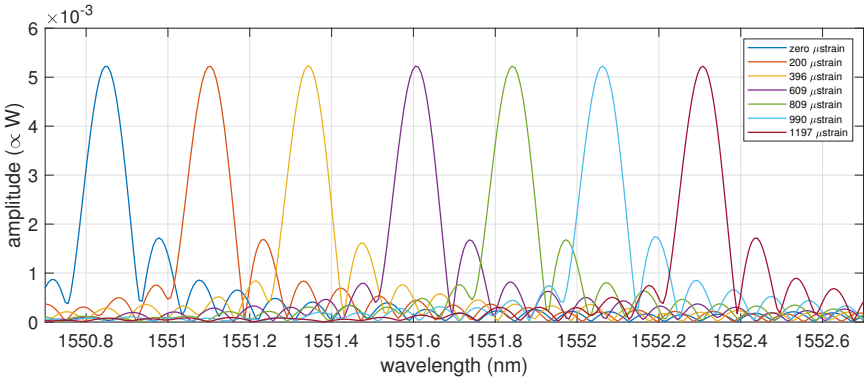

Figure 25. Reflection spectra (power vs. wavelength) of the FBG at 2.755 m along the sensing fiber for various dog-bone sample strain levels.

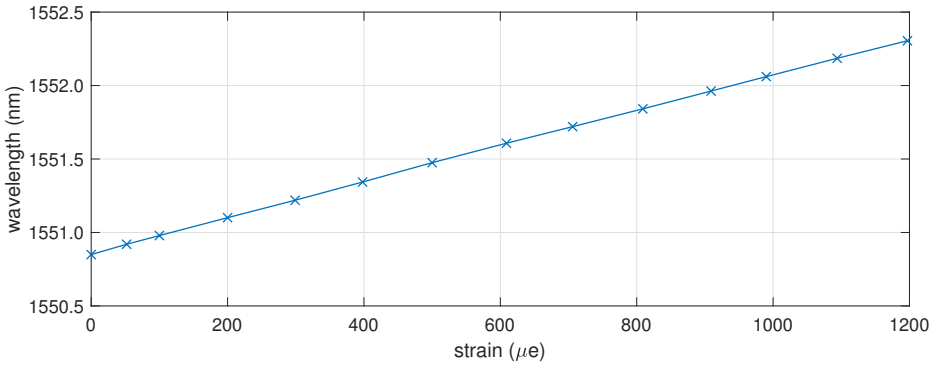

Figure 26. Bragg wavelengths of the FBG at 2.755 m along the sensing fiber vs. dog-bone sample strain.

A linear fit of the data in figure 26 gives a slope of 1.216x10^{-3} nm/μstrain (95% confidence interval = $\pm$8x10^{-6} nm/μstrain) and a zero intercept of 1550.858 nm (95% confidence interval = $\pm$5.5x10^{-3} nm). The gauge factor, $(1 - p_e)$, is then determined by dividing the slope ($\lambda_{B_0}(1 - p_e)$), by the zero intercept (λ_{B_0}), and is found to be 7.838x10^{-7} μstrain^{-1}, which is within 1/2 % the FBG supplier's specification of 7.8x10^{-7} μstrain^{-1} for the sensor's *strain sensitivity*. Inverting the slope of the linear fit shows that the FBG sensor requires 822.67 μstrain to induce a

1 nm change in Bragg wavelength. Applying the gauge factor to the measured Bragg wavelength shifts of 16 gratings along the dog bone sample while at maximum load gives the measured FBG sensor strain plot of figure 27. The grating strain data of

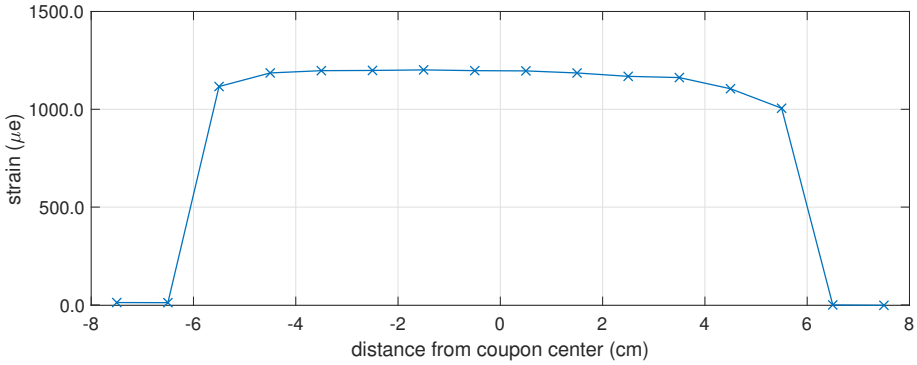

Figure 27. Measured strain of 16 FBG sensors along the dog-bone sample at maximum load: strain vs. distance from coupon center.

figure 27 shows an obvious differentiation between bonded gratings and non-bonded gratings, and the effects of bond-line edges are also observable. The non-symmetrical (length-wise) strain behavior along the coupon can be attributed to geometrical non-symmetry in the coupon and the sensing fiber not being perfectly aligned length-wise across the entirety of the bond-line.

6 System Design Trade-off Considerations

An OFDR FBG-based sensing system, as described in this paper, relies on a wavelength-sweep of a source laser to simultaneously illuminate a sensing fiber and an internal in-fiber reference interferometer. The return signal of the reference interferometer controls the sampling of the back-reflections from the sensing fiber, and the processing hardware of the OFDR subsequently executes signal processing of the sampled data set to yield the Bragg wavelengths of every grating along the sensing fiber. Typical architecture-specific performance parameters of interest for an FBG-based OFDR measurement system are measurement rate, raw data sampling rate, accuracy, and resolution, all of which are dependent upon the relationships between fiber length, laser tuning speed, spectral width, data size, and processing speed.

Measurement rate vs. laser tuning speed and spectral width

In this discussion, the term *measurement rate* refers to how many times a second an OFDR system wavelength-sweeps the source laser and outputs the Bragg wavelength of every grating along the sensing fiber. While it is very possible to interrogate a sensing fiber and formulate measurements in both an *up*-sweep (increasing wavelength) and a *down*-sweep (decreasing wavelength) of the laser wavelength, this discussion will assume data acquisition and measurement occur solely during the up-sweep of the laser. Because laser sweep rate is typically specified in terms of

wavelength (nm/s) and not wavenumber, this analysis will designate the variable λ_{lsr} to represent the wavelength sweep rate of the source laser in nm/s. In the case of a source laser using one sweep rate in both directions of wavelength sweep, the rate of measurement is the inverse of the time required for the laser to sweep up and back in wavelength. Designated as f_{meas}, the measurement rate is determined by

$$f_{meas} = \left(\frac{2 \times \lambda_{sw}}{\lambda_{lsr}} \right)^{-1}, \tag{47}$$

where λ_{sw} is the length of the wavelength band covered during data acquisition, or *spectral width* of the measurement. Note that in the previous example of strain sensing, it was shown that 1 nm of Bragg wavelength shift corresponds to ~ 823 μstrain. The measurement rate determination of eq. 47 and the associated curves shown in figure 28 can be recalculated to incorporate various sweep characteristics of a given laser. As an example, a laser may have the capability to have two different wave-

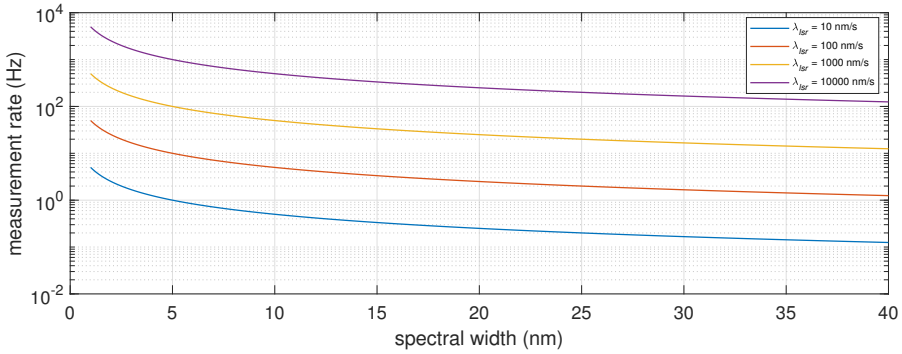

Figure 28. OFDR measurement rate vs. sweep spectral width for various laser sweep rates.

length sweep rates in the up and down directions. In such a case, if data is being sampled only in one direction, it may be desirable to bring the laser wavelength back to the starting position as quick as possible to ready the system for the next measurement cycle. There may also be some time delay between the end of a wavelength sweep in one direction and the beginning of a wavelength sweep in the opposite direction. Not included in eq. 47, however elementary to do so, are delays related to processing constraints.

Raw data sampling rate

The OFDR detection and sampling electronics of figure 5 illustrate the dependence of the raw data A/D module on the fringe spacing of the internal reference interferometer. As such, the minimum upper bandwidth of the detection/amplification electronics and the *sampling rate*, or *sampling frequency*, or *clocking frequency*, f_p of the A/D is directly dependent on the source laser's sweep rate λ_{lsr}, the length l_{ref} of the internal reference interferometer, and the effective index of refraction n of the fiber forming the reference interferometer. The derivation of an approximated raw data sampling rate follows.

Previously defined in Section 2, eq. 17, the wavenumber fringe spacing is dependent on the reference length using $k_\Delta = \pi / n l_{ref}$. To convert the fringe spacing to an approximate time interval, the sweep rate of the laser must be considered. Considering that the fringe spacing is the sampling basis interval $k_\Delta = k_1 - k_0$ and using the relationship $\lambda = 2\pi/k$ of eq. 2 leads to the defining of fringe spacing in terms of wavelength:

$$\frac{2\pi}{\lambda_1} - \frac{2\pi}{\lambda_0} = \frac{\pi}{n l_{ref}}. \tag{48}$$

Introducing a common denominator on the left of eq. 48 and rearranging leads to an explicit solution for the raw data set wavelength basis interval λ_Δ:

$$\lambda_\Delta = \lambda_0 - \lambda_1 = \frac{\lambda_0 \lambda_1}{2 n l_{ref}}. \tag{49}$$

For an OFDR operating around the typical wavelength range of 1550 nm, it is useful to assume $\lambda_0 \lambda_1 \approx (1550 \times 10^{-9})^2$ to allow for a simple, approximate solution. Dividing the wavelength sampling basis interval by laser sweep rate λ_{lsr} gives the time between consecutive raw data point sampling, and the sampling frequency is found via the inversion of the sampling time. The approximate raw data A/D clocking frequency f_p of an OFDR, as a function of the source laser's sweep rate λ_{lsr}, the length l_{ref} of the internal reference interferometer, and the effective index of refraction n of the fiber forming the reference interferometer, can thus be approximated using

$$f_p \approx \frac{2 n l_{ref} \lambda_{lsr} \times 10^{-9}}{(1550 \times 10^{-9})^2}. \tag{50}$$

In this particular derivation of OFDR sampling rate, the possibility of a negative value of λ_Δ is neglected, as sweeping of the laser wavelength up or down results in the same raw data sampling frequency. The approximated values of f_p vs. reference interferometer length for various laser sweep rates are plotted in figure 29. The effective index refraction n of the reference interferometer fiber is set to 1.4682 for this analysis.

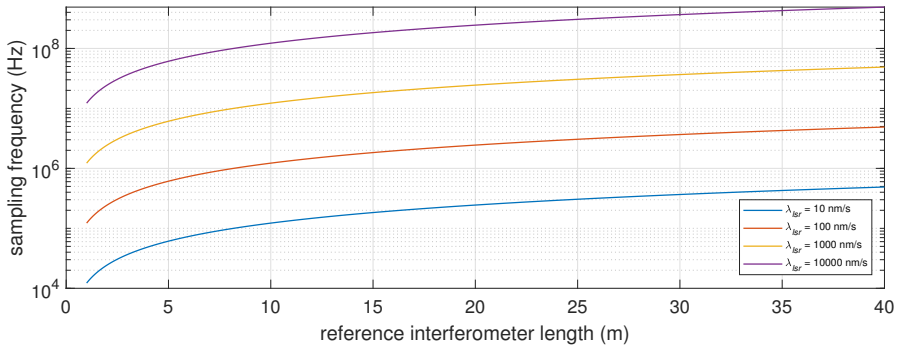

Figure 29. Raw data sampling frequency vs. reference interferometer length for various laser scan rates.

Resolution and Accuracy

Because the Bragg wavelengths are *calculated* from processed data (as opposed to directly measured), the resolution of an OFDR sensing system is theoretically infinitesimal. However, because an OFDR system is based on discrete sampling and processing of continuous phenomenon, noise in both the reference signal and the sensing signal will degrade the resolution and accuracy of an OFDR system. As such, it is critical to maintain as high a signal-to-noise ratio as possible through well-designed, low-noise detection and amplification electronics.

The configuration of the FBG sensors themselves may also affect accuracy. Examples of problematic sensor configurations include highly dynamic vibrating structures and the bonding of sensors onto surfaces which may experience high strain variations across areas which are smaller than the FBG physical length. An additional source of accuracy degradation is polarization misalignment between interfering electric fields. The interference signal produced by the combining of a reflected FBG electric field with the reflected field from the in-line broadband mirror can be degraded by the polarization misalignment of the two signals. The apparent varying amplitude of grating reflections seen in the measurement example of figure 21 is due to the varying polarization state of the light as it propagates through the sensing fiber. It is possible to have sufficient misalignment such that the FBG sensor signal of interest in the raw data is near zero, in which case measurement accuracy is significantly degraded. Not explored in this paper, the implementation of polarization diverse detection in an OFDR overcomes the polarization misalignment issue.

7 Conclusion

This paper serves as a basic manual for understanding, assembling, and utilizing an OFDR to perform measurements using FBG sensors. A basic OFDR signal model is derived, followed by an explanation of processing via simulation, a system component overview, a measurement example, and a brief discussion of basic parameters that can affect system speed, resolution, and accuracy. With the fundamental theory and signal processing of an OFDR understood, areas of further exploration and detailed discussions include polarization diverse detection, flight-hardening of hardware, dedicated DSP architectures for real-time OFDR measurement output, vibration effects in OFDR-FBG signals, the effects of non-uniform environmental effects along the length of an FBG sensor, and the adaptation of the signal models and processing methodology to enable fiber optic sensing based on Rayleigh scattering.

References

1. K. Hill, Y. Fujii, D. C. Johnson, and B. Kawasaki, "Photosensitivity in optical fiber waveguides: Application to reflection filter fabrication," Applied physics letters, vol. 32, no. 10, pp. 647–649, 1978.

2. G. Meltz, W. Morey, and W. Glenn, "Formation of bragg gratings in optical fibers by a transverse holographic method," Optics letters, vol. 14, no. 15, pp. 823–825, 1989.

3. R. Kashyap, Fiber bragg gratings. Academic press, 2009.

4. A. Cusano, A. Cutolo, and J. Albert, Fiber Bragg grating sensors: recent advancements, industrial applications and market exploitation. Bentham Science Publishers, 2011.

5. A. D. Kersey, M. A. Davis, H. J. Patrick, M. LeBlanc, K. Koo, C. Askins, M. Putnam, and E. J. Friebele, "Fiber grating sensors," Journal of lightwave technology, vol. 15, no. 8, pp. 1442–1463, 1997.

6. M. E. Froggatt, "Apparatus and method for measuring strain in bragg gratings," Aug. 25 1998, uS Patent 5,798,521.

7. B. A. Childers, M. E. Froggatt, S. G. Allison, T. C. Moore Sr, D. A. Hare, C. F. Batten, and D. C. Jegley, "Use of 3000 bragg grating strain sensors distributed on four 8-m optical fibers during static load tests of a composite structure," in Smart structures and materials 2001: Industrial and commercial applications of smart structures technologies, vol. 4332. SPIE, 2001, pp. 133–142.

8. R. Beemer, M. Cassidy, and C. Gaudin, "Investigation of an ofdr fibre bragg system for use in geotechnical scale modelling," in Physical Modelling in Geotechnics, Volume 1: Proceedings of the 9th International Conference on Physical Modelling in Geotechnics (ICPMG 2018), July 17-20, 2018, London, United Kingdom. CRC Press, 2018, p. 279.

9. B. J. Soller, D. K. Gifford, M. S. Wolfe, and M. E. Froggatt, "High resolution optical frequency domain reflectometry for characterization of components and assemblies," Optics Express, vol. 13, no. 2, pp. 666–674, 2005.

10. H. Kogelnik, "Filter response of nonuniform almost-periodic structures," Bell System Technical Journal, vol. 55, no. 1, pp. 109–126, 1976.

11. (2023). [Online]. Available: https://fbgs.com/components/all-grating-fibers-agf/

12. A. Othonos and K. Kalli, Fiber Bragg Gratings: Fundamentals and Applications in Telecommunications and Sensing. Artech House, 1999.

Appendix A. List of variables

variable	description
δ	wave phase offset
ε	axial strain
λ	wavelength
λ_Δ	raw data set basis interval in wavelength
λ_0	raw data set start wavelength
λ_B	FBG Bragg wavelength
λ_{B_0}	zero-strain, or baseline, FBG Bragg wavelength in a strain measurement application
λ_{lsr}	source laser wavelength sweep rate
λ_{sw}	data acquisition spectral width
ω	angular frequency
E	electric field representation of a monochromatic plane wave
E_0	electric field amplitude
E_s	electric field representation of light at the sensing leg detector face
E_{det}	electric field representation of light at a detector face
E_{ref}	electric field representation of light at the reference leg detector face
f	frequency
$f_B(k)$	FBG reflection function; FBG reflection spectrum; FBG spectral response
$f_{B_m}(k)$	specification of $f_B(k)$ for FBG number m in a sensing fiber
f_{meas}	system measurement rate
f_p	raw data sampling rate; raw data sampling frequency; raw data A/D clocking frequency
$G_{m,j}(z)$	FBG number m to FBG number j cross-convolution function
I	time-average intensity
k	free space wavenumber; raw data set basis
k_Δ	wavenumber fringe spacing of an interferometer; raw data set basis
k_0	raw data set start wavenumber
k_B	FBG Bragg wavenumber
k_{B_m}	specification of k_B for FBG number m in a sensing fiber
k_{B_Δ}	wavenumber difference between FBG number m and FBG number j
$\tilde{k}$	FBG spectral set wavenumber basis
$\tilde{k}_\Delta$	spectral set basis interval
L_B	FBG length
L_{B_m}	specification of L_B for FBG number m in a sensing fiber
l	physical fiber length difference between two legs of a simple in-fiber Michelson interferometer
l_B	length difference of the sensing interferometer; location of an FBG in the sensing fiber relative to mirror M0
l_{B_m}	specification of l_B for FBG number m in a sensing fiber; location of FBG number m in the sensing fiber relative to mirror M0

l_{ref}	length difference of the reference interferometer
M	number of FBG sensors in a sensing fiber
n	fiber effective index of refraction
N	raw data set sample size
$\tilde{N}$	FBG spectral set size
P	power
P_0	power of light having electric field amplitude E_0
P_{det}	power of light at detector face
$P\,[z]$	spatial set
$P_B[z]$	windowed FBG spatial set
P_{ref}	power of light at the reference leg detector face
P_s	power of light at the sensing leg detector face
$p\,[k]$	raw data set; sensing fiber sampled set
$\tilde{p}[\tilde{k}]$	FBG spectral set
p_e	effective strain-optic constant
R_0, R_1, R_2	power reflection coefficient of reflectors R0, R1, and R2, respectively
R_B	FBG peak power reflection coefficient
R_{B_m}	specification of R_B for FBG number m in a sensing fiber
t	time
z	axial distance along a fiber; spatial set basis
z_s	total physical traverse length of a light wave from laser to detector
z_Δ	real-world spatial set basis interval; spatial resolution
$\tilde{z}_\Delta$	spatial set basis interval

Appendix B. Signal Derivations

B.1 Michelson interferometer signal

The total electric field arriving at the detector is represented by

$$E_{det} = \frac{1}{2}E_0(e^{i(knz_s-\pi)} + e^{i(kn(z_s+2l)-\pi)}) \tag{B1}$$

and can be rewritten as

$$E_{det} = \frac{1}{2}E_0 e^{-i\pi}(e^{iknz_s} + e^{i(kn(z_s+2l))}). \tag{B2}$$

Using $P \propto EE^*$ yields

$$\begin{aligned}
P_{det} &\propto E_{det}E_{det}^* \\
P_{det} &\propto \frac{1}{4}E_0^2 e^{-i\pi}e^{i\pi}(e^{ikn(z_s)} + e^{ikn(z_s+2l)})(e^{-ikn(z_s)} + e^{-ikn(z_s+2l)}) \\
P_{det} &\propto \frac{1}{4}E_0^2(1+1+e^{ikn(z_s-z_s-2l)} + e^{ikn(z_s+2l-z_s)}) \\
P_{det} &\propto \frac{1}{2}E_0^2(1+\cos(2knl)).
\end{aligned} \tag{B3}$$

B.2 Signal from sensing fiber with multiple gratings

The total electric field at the sensing leg photodetector is represented by

$$\frac{1}{\sqrt{2}}E_0\left(\sqrt{R_0} + (1-R_0)\sum_{m=1}^{M} f_{B_m}(k)e^{ik2nl_{B_m}}\right). \tag{B4}$$

Using $P \propto EE^*$ and eliminating common multiplier $\frac{1}{\sqrt{2}}E_0$ gives

$$\begin{aligned}
P_s \propto \left(\sqrt{R_0} + (1-R_0)\sum_{m=1}^{M} f_{B_m}(k)e^{ik2nl_{B_m}}\right) \times \\
\left(\sqrt{R_0} + (1-R_0)\sum_{m=1}^{M} f_{B_m}(k)e^{-ik2nl_{B_m}}\right).
\end{aligned} \tag{B5}$$

Multiplying terms through yields

$$\begin{aligned}
P_s \propto R_0 + \sqrt{R_0}(1-R_0)\sum_{m=1}^{M} f_{B_m}(k)e^{-ik2nl_{B_m}} + \sqrt{R_0}(1-R_0)\sum_{m=1}^{M} f_{B_m}(k)e^{ik2nl_{B_m}} + \\
(1-R_0)^2\sum_{m=1}^{M} f_{B_m}(k)e^{ik2nl_{B_m}}\sum_{m=1}^{M} f_{B_m}(k)e^{-ik2nl_{B_m}}.
\end{aligned} \tag{B6}$$

Separating out the terms of the double-sum for which $m = j$ yields

$$P_s \propto R_0 + 2\sqrt{R_0}(1-R_0)\sum_{m=1}^{M} f_{B_m}(k)\cos(k2nl_{B_m}) + \\ (1-R_0)^2\sum_{m=1}^{M} f_{B_m}^2(k) + (1-R_0)^2\sum_{m=1}^{M}\sum_{\substack{j=1 \\ j\neq m}}^{M} f_{B_m}(k)f_{B_j}(k)e^{ik2n(l_{B_m}-l_{B_j})}. \quad \text{(B7)}$$

Equation B7 contains a complex exponential in the double-sum that is eliminated via symmetry. Given a pair of integers $[a, b]$ the following it true:

$$l_{B_{m=a}} - l_{B_{j=b}} = -\left(l_{B_{m=b}} - l_{B_{j=a}}\right). \quad \text{(B8)}$$

Then for $a \neq b$ terms in the double sum can be paired according to $[a, b]$:

$$f_{B_{m=a}}(k)f_{B_{j=b}}(k)e^{ik2n(l_{B_{m=a}}-l_{B_{j=b}})} + f_{B_{m=b}}(k)f_{B_{j=a}}(k)e^{ik2n(l_{B_{m=b}}-l_{B_{j=a}})}. \quad \text{(B9)}$$

Applying the symmetry of eq. B8 leads to reordering the paired terms as

$$f_{B_a}(k)f_{B_b}(k)\left(e^{ik2n(l_{B_a}-l_{B_b})} + e^{-ik2n(l_{B_a}-l_{B_b})}\right), \quad \text{(B10)}$$

which reduces to

$$2f_{B_a}(k)f_{B_b}(k)\cos\left(k2n(l_{B_a} - l_{B_b})\right). \quad \text{(B11)}$$

Including the reduction result of eq. B11 to rewrite the double-sum term in eq. B7 gives the final representation of the signal as

$$P_s \propto R_0 + 2\sqrt{R_0}(1-R_0)\sum_{m=1}^{M} f_{B_m}(k)\cos\left(2knl_{B_m}\right) + (1-R_0)^2\sum_{m=1}^{M} f_{B_m}^2(k) + \\ 2(1-R_0)^2\sum_{m=1}^{M-1}\sum_{j=m+1}^{M} f_{B_m}(k)f_{B_j}(k)\cos\left(2kn(l_{B_j} - l_{B_m})\right). \quad \text{(B12)}$$

Appendix C. Fourier Transform Derivations

C.1 Useful Fourier transform properties and pairs

Given function $g(k)$, define the Fourier transform of $g(k)$ as:

$$\mathcal{F}\{g(k)\} = G(z) = \frac{1}{\sqrt{2\pi}} \int_{-\infty}^{\infty} g(k) e^{-izk} dk \tag{C1}$$

and the inverse Fourier transform as:

$$\mathcal{F}^{-1}\{G(z)\} = g(k) = \frac{1}{\sqrt{2\pi}} \int_{-\infty}^{\infty} G(z) e^{izk} dz \tag{C2}$$

Fourier transform of a rectangle function:

$$\mathcal{F}\{\text{rect}(ak)\} = \frac{1}{\sqrt{2\pi a^2}} \text{sinc}\left(\frac{z}{2\pi a}\right) \tag{C3}$$

Fourier transform of a sinc function:

$$\mathcal{F}\{\text{sinc}(ak)\} = \frac{1}{\sqrt{2\pi a^2}} \text{rect}\left(\frac{z}{2\pi a}\right) \tag{C4}$$

Fourier transform of a squared sinc function:

$$\mathcal{F}\left\{\text{sinc}^2(ak)\right\} = \frac{1}{\sqrt{2\pi a^2}} \text{tri}\left(\frac{z}{2\pi a}\right) \tag{C5}$$

Fourier transform of a cosine:

$$\mathcal{F}\{\cos(z_0 k)\} = \pi\left[\delta(z + z_0) + \delta(z - z_0)\right] \tag{C6}$$

Time-shift Fourier transform property:

$$\mathcal{F}\{g(k - a)\} = e^{-iaz} G(z) \tag{C7}$$

Fourier transform convolution theorem:

$$\mathcal{F}\{g(k)h(k)\} = \frac{(G * H)(z)}{\sqrt{2\pi}} \tag{C8}$$

C.2 Response function of a low-reflectivity fiber Bragg grating

Consider an optical fiber containing a Bragg Grating with a periodically-modulated index structure that begins at length $-L_B/2$ and ends at length $L_B/2$, and has spatial periodicity, or grating *pitch*, Λ along the length z of a fiber with effective index of refraction n. The resonant, or *Bragg*, reflection wavelength of the grating is set by

$$\lambda_B = 2n\Lambda \tag{C9}$$

and the associated Bragg wavenumber is

$$k_B = \frac{2\pi}{\lambda_B}. \tag{C10}$$

The normalized envelope of the periodically-modulated index perturbation function of the grating can be represented as

$$\kappa(z) = \text{rect}\left(\frac{z}{L_B}\right). \tag{C11}$$

For a deviation from the resonant Bragg condition of the grating defined by

$$\varphi = k - k_B, \tag{C12}$$

the response ρ of the grating for wavenumbers at or near the Bragg resonance condition can be approximated by

$$\rho(\varphi) = \mathcal{F}\left\{\kappa(z)\right\}. \tag{C13}$$

Applying the Fourier transform pair of eq. C3 to eq. C11 leads to the following grating response approximation:

$$\rho(k - k_B) = \frac{L_B}{2}\,\text{sinc}\left(\frac{L_B(k - k_B)}{2\pi}\right). \tag{C14}$$

The goal of this derivation is to approximate the grating response function $f_B(k)$, which is accomplished by Fourier transforming of the index perturbation function of the fiber grating section. The peak amplitude of the response function was not determined because a *normalized* envelope function was used in the derivation. In place of a derived peak amplitude of response, the term $\sqrt{R_B}$ will be used, where R_B is the peak reflectivity of the FBG reflectivity function. Additionally, because the OFDR interferometric method scales all fiber lengths by $2n$, the length, L_B, of the grating will also be scaled accordingly in the approximated response function. The final result of the derivation is an FBG response function that is approximated by the Fourier transform of the index perturbation function with an arbitrary peak response:

$$f_B(k) \approx \sqrt{R_B}\,\text{sinc}\left(\frac{2nL_B(k - k_B)}{2\pi}\right) \tag{C15}$$

C.3 Fourier transform of squared sinc term

The third term of eq. 28 is a summation of

$$(1 - R_0)^2 R_B\,\text{sinc}^2\left(\frac{2nL_B(k - k_{B_m})}{2\pi}\right). \tag{C16}$$

Applying the time-shift Fourier transform property of eq. C7 to the Fourier transform pair of eq. C5 yields

$$\frac{\sqrt{2\pi}(1 - R_0)^2 R_B}{2nL_B} e^{-ik_{B_m}z}\,\text{tri}\left(\frac{z}{2nL_B}\right). \tag{C17}$$

Reincorporating the summation notation yields

$$\frac{\sqrt{2\pi}(1-R_0)^2 R_B}{2nL_B} \sum_{m=1}^{M} e^{-ik_{B_m} z} \operatorname{tri}\left(\frac{z}{2nL_B}\right). \tag{C18}$$

C.4 Fourier transform of sinc-modulated sinusoid term

The second term of eq. 28 is a summation of

$$2(1-R_0)\sqrt{R_0 R_B}\operatorname{sinc}\left(\frac{2nL_B(k-k_{B_m})}{2\pi}\right)\cos(2knl_{B_m}). \tag{C19}$$

Applying the time-shift Fourier transform property of eq. C7 and the Fourier transform convolution theorem of eq. C8 to the Fourier transform pairs of eqs. C4 and C6 (positive fiber lengths only) yields the Fourier transform result of eq. C19 as

$$\pi\,(1-R_0)\,\sqrt{R_0 R_B} e^{-ik_{B_m}(z-2nl_{B_m})} \operatorname{rect}\left(\frac{z-2nl_{B_m}}{2nL_B}\right). \tag{C20}$$

Reincorporating the summation notation yields

$$\pi\,(1-R_0)\,\sqrt{R_B R_0} \sum_{m=1}^{M} e^{-ik_{B_m}(z-2nl_{B_m})} \operatorname{rect}\left(\frac{z-2nl_{B_m}}{2nL_B}\right). \tag{C21}$$

C.5 Fourier transform of multiple grating double-sum term

The term in the double-sum of eq. 28 was shown to be

$$2(1-R_0)^2 R_B \operatorname{sinc}\left(\frac{2nL_B(k-k_{B_m})}{2\pi}\right)\operatorname{sinc}\left(\frac{2nL_B(k-k_{B_j})}{2\pi}\right)\cos\left(2kn(l_{B_j}-l_{B_m})\right) \tag{C22}$$

The two-function Fourier transform convolution theorem of eq. C8 is applied to the Fourier transform of a three-function product as

$$\mathcal{F}\left\{g_1(k)g_2(k)g_3(k)\right\} = \frac{(G_1 * G_2 * G_3)(z)}{2\pi} \tag{C23}$$

and the three different wavenumber-dependent functions of eq. C22 are defined as

$$g_1(k) = \operatorname{sinc}\left(\frac{2nL_B(k-k_{B_m})}{2\pi}\right) \tag{C24}$$

$$g_2(k) = \operatorname{sinc}\left(\frac{2nL_B(k-k_{B_j})}{2\pi}\right) \tag{C25}$$

$$g_3(k) = \cos\left(2kn(l_{B_j}-l_{B_m})\right) \tag{C26}$$

Using the Fourier transform for a sinc function as in eq. C4 and the time shift property of eq. C7 yields

$$G_1(z) = \frac{\sqrt{2\pi}}{2nL_B} \operatorname{rect}\left(\frac{z}{2nL_B}\right) e^{-ik_{B_m} z}; \tag{C27}$$

$$G_2(z) = \frac{\sqrt{2\pi}}{2nL_B}\,\mathrm{rect}\left(\frac{z}{2nL_B}\right)e^{-ik_{B_j}z}. \tag{C28}$$

Using the Fourier transform for a cosine function as in eq. C6 and considering only positive fiber lengths yields

$$G_3(z) = \pi\left(\delta(z - 2n(l_{B_j} - l_{B_m}))\right) \tag{C29}$$

The convolution $(G_1 * G_2)(z)$ is explicitly defined as

$$G_1 * G_2(z) = \frac{\pi}{2n^2L_B^2}\times \int_{-\infty}^{\infty}\mathrm{rect}\left(\frac{z-\tau}{2nL_B}\right)e^{-ik_{B_m}(z-\tau)}\,\mathrm{rect}\left(\frac{\tau}{2nL_B}\right)e^{-ik_{B_j}\tau}d\tau. \tag{C30}$$

Rearranging the exponential terms yields:

$$G_1 * G_2(z) = \frac{\pi}{2n^2L_B^2}\times e^{-ik_{B_m}z}\int_{-\infty}^{\infty}\mathrm{rect}\left(\frac{z-\tau}{2nL_B}\right)\mathrm{rect}\left(\frac{\tau}{2nL_B}\right)e^{-i\tau(k_{B_j}-k_{B_m})}d\tau. \tag{C31}$$

It is clear from eq. C31 that if two gratings have identical Bragg wavenumbers ($k_{B_m} = k_{B_j}$), the exponent term inside the integral is unity and the result is the convolution of two identical rect functions, resulting in a triangle function (in z) with total width $4nL_B$, centered at distance $z = 0$, of a maximum amplitude of $(2nL_B)^{-2}$. Additionally, in this case, the phase of the triangle function vs. z is dependent on the Bragg wavenumber. In practical application, gratings will have Bragg wavenumber values that are not precisely equal. The evaluation of the convolution integral for the more likely scenario of unequal Bragg wavenumber among gratings ($k_{B_m} \neq k_{B_j}$) is more complicated than simple convolution of two identical rectangle functions, but the result of the integral can be partially explored here to determine the qualitative aspects of the result. Limiting the integral evaluation interval to only the range in which the second rect function is non-zero ($|\tau| \leq nL_B$) gives

$$e^{-ik_{B_m}z}\int_{-nL_B}^{nL_B}\mathrm{rect}\left(\frac{z-\tau}{2nL_B}\right)e^{-i\tau(k_{B_j}-k_{B_m}))}d\tau. \tag{C32}$$

The rectangle function in the integral is dependent on both z and τ and is non-zero only for $|z - \tau| \leq nL_B$. The evaluation of the definite integral,therefore, has two sets of interval limits, depending on the value of z. For $-2nL_B \leq z \leq 0$ the integral is evaluated from $-nL_B$ to $z + nL_B$. For $0 < z \leq 2nL_B$ the integral is evaluated from $z - nL_B$ to nL_B. Applying the interval limits accordingly yields

$$e^{-ik_{B_m}z}\int_{-nL_B}^{z+nL_B}e^{-i\tau(k_{B_j}-k_{B_m})}d\tau; -2nL_B \leq z \leq 0 \tag{C33}$$

$$e^{-ik_{B_m}z}\int_{z-nL_B}^{nL_B}e^{-i\tau(k_{B_j}-k_{B_m})}d\tau; 0 < z \leq 2nL_B \tag{C34}$$

The explicit integration notation is

$$\frac{e^{-ik_{B_m}z}e^{-i\tau(k_{B_j}-k_{B_m})}}{-i(k_{B_j}-k_{B_m})}\Bigg|_{-nL_B}^{z+nL_B};-2nL_B\leq z\leq 0 \tag{C35}$$

$$\frac{e^{-ik_{B_m}z}e^{-i\tau(k_{B_j}-k_{B_m})}}{-i(k_{B_j}-k_{B_m})}\Bigg|_{z-nL_B}^{nL_B};0<z\leq 2nL_B \tag{C36}$$

Inserting the definite integral limits and using $k_{B_\Delta}=k_{B_j}-k_{B_m}$ gives

$$\frac{e^{-ik_{B_m}z}(e^{-i(z+nL_B)k_{B_\Delta}}-e^{-i(-nL_B)k_{B_\Delta}})}{-ik_{B_\Delta}};-2nL_B\leq z\leq 0 \tag{C37}$$

$$\frac{e^{-ik_{B_m}z}(e^{-i(nL_B)k_{B_\Delta}}-e^{-i(z-nL_B)k_{B_\Delta}})}{-ik_{B_\Delta}};0<z\leq 2nL_B \tag{C38}$$

Firstly, eqs. C37 and C38 sum to zero at $z=-2nL_B$ and $z=2nL_B$, respectively, and have decreasing amplitude as the Bragg wavenumber difference between gratings increases. This is expected since the farther apart two gratings are in wavenumber, the less they will interfere/interact with each other in the spectral domain. Secondly, although the two equations show decreasing amplitude with increasing grating length L_B, grating reflection strength typically increases with grating length, and the increased amplitude would be realized in the multiplier of eq. C22 where R_B is in the numerator. Thirdly, as previously discussed, when k_{B_Δ} is zero, the convolution of the two rectangle functions converges into a triangle function of z with width $4nL_B$. However, as k_{B_Δ} increases, the convolution result shows spreading of amplitude between $\pm 2nL_B$ and increasing oscillatory amplitude as the various phase terms become more oscillatory. Finally, both equations have k_{B_Δ} in the denominator, which would seem to be an issue should two gratings have equal Bragg wavenumber. However, expanding the complex exponential representation into rectangular coordinates and implementing trigonometric assumptions as $k_B\Delta$ goes to zero results in k_{B_Δ} factoring out of the equation, therefore eliminating the issue of zero in the denominator. Numerical simulations in which raw data with precisely equal Bragg wavenumber is Fourier transformed to spatial data reveal a triangle function of z for these particular terms, as previously discussed, proving that there is no issue of zero in the denominator when Fourier transforming the raw data. To continue with the development of the Fourier transform of the multiple grating double-sum term, eqs. C37 and C38 will be given the representation $G_{m,j}(z)$:

$$G_{m,j}(z)=\begin{cases}\frac{e^{-ik_{B_m}z}(e^{-i(z+nL_B)k_{B_\Delta}}-e^{-i(-nL_B)k_{B_\Delta}})}{-ik_{B_\Delta}} & \text{if } -2nL_B\leq z\leq 0\\ \frac{e^{-ik_{B_m}z}(e^{-i(nL_B)k_{B_\Delta}}-e^{-i(z-nL_B)k_{B_\Delta}})}{-ik_{B_\Delta}} & \text{if } 0<z\leq 2nL_B\\ 0 & \text{otherwise}\end{cases} \tag{C39}$$

The final step to complete the Fourier transform derivation of the multiple grating double-sum term is the convolution of $G_{m,j}(z)$ with $G_3(z)=\pi\left(\delta(z-2n(l_{B_j}-l_{B_m}))\right)$

from eq. C29, which results in a shift in z to $2n(l_{B_j} - l_{B_m})$. Bringing the two convolution results together to complete the Fourier transform of the multiple grating double sum term is expressed as

$$\begin{aligned}\frac{(G_1 * G_2 * G_3)(z)}{2\pi} &= \frac{1}{2\pi} \cdot 2(1-R_0)^2 R_B \cdot \frac{\pi}{2n^2 L_B^2} \cdot G_{m,j}(z) \\ &= \frac{R_B(1-R_0)^2}{2n^2 L_B^2} G_{m,j}(z) \end{aligned} \tag{C40}$$

and the shift in z is now included in the specification of $G_{m,j}(z)$ as

$$G_{m,j}(z) = \begin{cases} \frac{e^{-ik_{B_m}z}(e^{-i(z+nL_B)k_{B_\Delta}} - e^{-i(-nL_B)k_{B_\Delta}})}{-ik_{B_\Delta}} & \text{if } -2nL_B \le z - 2n(l_{B_j} - l_{B_m}) \le 0 \\ \frac{e^{-ik_{B_m}z}(e^{-i(nL_B)k_{B_\Delta}} - e^{-i(z-nL_B)k_{B_\Delta}})}{-ik_{B_\Delta}} & \text{if } 0 < z - 2n(l_{B_j} - l_{B_m}) \le 2nL_B \\ 0 & \text{otherwise} \end{cases} \tag{C41}$$

Appendix D. Sensing Fiber Specifications

Reflectivity	$< 0.1\%$
FBG center wavelength (approximate)	1550.85 nm
FBG length	9 mm
Attenuation @ 1550 nm	< 8.6 dB/km
Mode Field Diameter (MFD) @ 1550 nm	6 μm (typical)
Numerical Aperture (NA)	0.26 (typical)
Cladding diameter	125 μm $\pm$ 1 μm
Coating type	single layer acrylate
Coated fiber diameter	195 μm (typical)
Tensile load at break	> 50 N
Temperature sensitivity (formula: $\Delta\lambda/(\lambda \cdot \Delta T)$)	$6.5K^{-1} \cdot 10^{-6}$ (typical)
Strain sensitivity (formula: $\Delta\lambda/(\lambda \cdot \Delta\varepsilon)$	$7.8\mu\varepsilon^{-1} \cdot 10^{-7}$ (typical)

Table D1. Sensing fiber specifications [11]

REPORT DOCUMENTATION PAGE	Form Approved OMB No. 0704–0188

1. REPORT DATE *(DD-MM-YYYY)*	2. REPORT TYPE	3. DATES COVERED *(From - To)*
01-05-2023	Technical Publication	

4. TITLE AND SUBTITLE
Basic Theory and Operating Principles of Optical Frequency Domain Reflectometry Measurement Systems as Applied to Fiber Bragg Grating Sensors

5a. CONTRACT NUMBER

5b. GRANT NUMBER

5c. PROGRAM ELEMENT NUMBER

6. AUTHOR(S)
Jason P. Moore

5d. PROJECT NUMBER

5e. TASK NUMBER

5f. WORK UNIT NUMBER

7. PERFORMING ORGANIZATION NAME(S) AND ADDRESS(ES)
NASA Langley Research Center
Hampton, Virginia 23681-2199

8. PERFORMING ORGANIZATION REPORT NUMBER

9. SPONSORING/MONITORING AGENCY NAME(S) AND ADDRESS(ES)
National Aeronautics and Space Administration
Washington, DC 20546-0001

10. SPONSOR/MONITOR'S ACRONYM(S)
NASA

11. SPONSOR/MONITOR'S REPORT NUMBER(S)
NASA/TP–20230005269

12. DISTRIBUTION/AVAILABILITY STATEMENT
Unclassified-Unlimited
Subject Category
Availability: NASA STI Program (757) 864-9658

13. SUPPLEMENTARY NOTES
An electronic version can be found at http://ntrs.nasa.gov.

14. ABSTRACT

Optical frequency domain reflectometer (OFDR) systems provide for the interrogation of hundreds of fiber Bragg gratings (FBGs) within a single optical fiber. The coupling of FBG sensors to an OFDR interrogator results in a highly-distributed measurement system utilizing sensors that are lightweight, immune to electromagnetic interference, and low-profile. This paper presents and explores a basic derivation of OFDR-FBG signals, the processing of those signals, the assembly of a basic OFDR system, an example measurement scenario, and the effects of specific component and configuration changes on interrogator speed, resolution, and accuracy.

15. SUBJECT TERMS
optical frequency domain reflectometry, fiber Bragg gratings, fiber optic sensors, OFDR, FBG

16. SECURITY CLASSIFICATION OF:			17. LIMITATION OF ABSTRACT	18. NUMBER OF PAGES	19a. NAME OF RESPONSIBLE PERSON
a. REPORT	b. ABSTRACT	c. THIS PAGE			STI Information Desk (help@sti.nasa.gov)
U	U	U	UU	48	19b. TELEPHONE NUMBER *(Include area code)* (757) 864-9658